3 An Analytical Model for Tropical Cyclone Outer-Size Expansion on the f Plane

DANYANG WANG® AND DANIEL R. CHAVAS®

^a Department of Earth, Atmospheric, and Planetary Sciences, Purdue University, West Lafayette, Indiana

(Manuscript received 10 May 2023, in final form 6 March 2024, accepted 7 April 2024)

ABSTRACT: Tropical cyclones are known to expand to an equilibrium size on the f plane, but the expansion process is not understood. In this study, an analytical model for tropical cyclone outer-size expansion on the f plane is proposed. Conceptually, the storm expands because the imbalance between latent heating and radiative cooling drives a lateral inflow that imports absolute vorticity. Volume-integrated latent heating increases more slowly with size than radiative cooling, and hence, the storm expands toward an equilibrium size. The predicted expansion rate is given by the ratio of the difference in size from its equilibrium value $r_{t,eq}$ to an environmentally determined time scale τ_{rt} of 10–15 days. The model is fully predictive if given a constant $r_{t,eq}$, which can also be estimated environmentally. The model successfully captures the first-order size evolution across a range of numerical simulation experiments in which the potential intensity and f are varied. The model predictions of the dependencies of lateral inflow velocity and expansion rate on latent heating rate are also compared well with numerical simulations. This model provides a useful foundation for understanding storm size dynamics in nature.

KEYWORDS: Atmosphere; Hurricanes/typhoons; Tropical cyclones; Entropy

1. Introduction

Tropical cyclone (TC) outer size is known to expand with time toward an equilibrium size in idealized simulations on the f plane (Chan and Chan 2014, 2015; Chavas and Emanuel 2014; Martinez et al. 2020). Expansion with time is also seen in reanalysis or simulations on spherical geometry (Schenkel et al. 2018, 2023). Reanalysis data show that the median expansion rate of TC outer radius (of 8 m s⁻¹ near-surface wind) is tens of kilometers per day, with extreme cases being hundreds of kilometers per day (Schenkel et al. 2023). Although TC intensity and intensification have been understood with the help of some relatively well-established analytical theories (Emanuel 1986, 2012; Emanuel and Rotunno 2011; Wang et al. 2021a,b), a conceptual understanding of tropical cyclone size and size expansion is not as complete. Although theoretical models link inner size (radius of maximum wind) to outer size (Emanuel and Rotunno 2011; Chavas and Lin 2016), the mechanism of the changes in inner and outer sizes is not the same (Weatherford and Gray 1988; Chavas and Knaff 2022); the present study will focus on the TC outersize-expansion mechanism.

Recently, Wang et al. (2022) proposed a model for tropical cyclone potential size (TC PS) on the f plane that explains equilibrium TC size and is solely dependent on environmental parameters. The model yields a new scaling that is similar to

Corresponding author: Danyang Wang, wang 5571@purdue.edu

the length scale V_p/f , where V_p is the potential intensity and f is the Coriolis parameter, proposed in prior work (Chavas and Emanuel 2014). The TC PS model combines the Carnot cycle model for the energetics of a TC (Emanuel 1988, 1991) and a model for the complete low-level TC wind field (Chavas et al. 2015) to solve for an equilibrium size based on the most efficient thermodynamic cycle. However, such a method does not provide a description of how other parts of the TC are working, without which the potential size may not be achieved at all. It is also unsatisfying that the thermodynamic cycle is formulated in steady state so that it does not mechanistically explain how and why a TC expands toward equilibrium. Although the model suggests that an energy surplus exists when a TC is smaller than its potential size, it cannot explain how this energy surplus might drive expansion.

Previous studies on TC size expansion consistently note the importance of low-level inflow for bringing environmental absolute angular momentum inward to drive expansion (Hill and Lackmann 2009; Bui et al. 2009; Wang 2009; Chan and Chan 2014, 2015, 2018; Martinez et al. 2020; Wang and Toumi 2022), which is a direct reflection of the spinup of the outercore wind field. The TC size-expansion rate has been further found to depend on initial vortex size (Xu and Wang 2010; Chan and Chan 2014; Martinez et al. 2020) and rainband activity (Hill and Lackmann 2009; Wang 2009; Fudeyasu et al. 2010; Martinez et al. 2020), as well as cloud radiative forcing (Bu et al. 2014, 2017). Simulations have also shown that TC size is able to continue expanding substantially long after intensity becomes quasi-steady (Hill and Lackmann 2009; Chan and Chan 2014, 2015; Martinez et al. 2020). However, a simple universal understanding of why a TC should expand, how fast, why size should approach an equilibrium, and how this behavior depends on environmental parameters is still lacking. This is partly because the lateral inflow or import of absolute angular momentum has yet to be fully and quantitatively linked to environmental parameters and internal processes.

DOI: 10.1175/JAS-D-23-0088.1

Openotes content that is immediately available upon publication as open access.

Supplemental information related to this paper is available at the Journals Online website: https://doi.org/10.1175/JAS-D-23-0088.s1.

^{© 2024} American Meteorological Society. This published article is licensed under the terms of the default AMS reuse license. For information regarding reuse of this content and general copyright information, consult the AMS Copyright Policy (www.ametsoc.org/PUBSReuseLicenses).

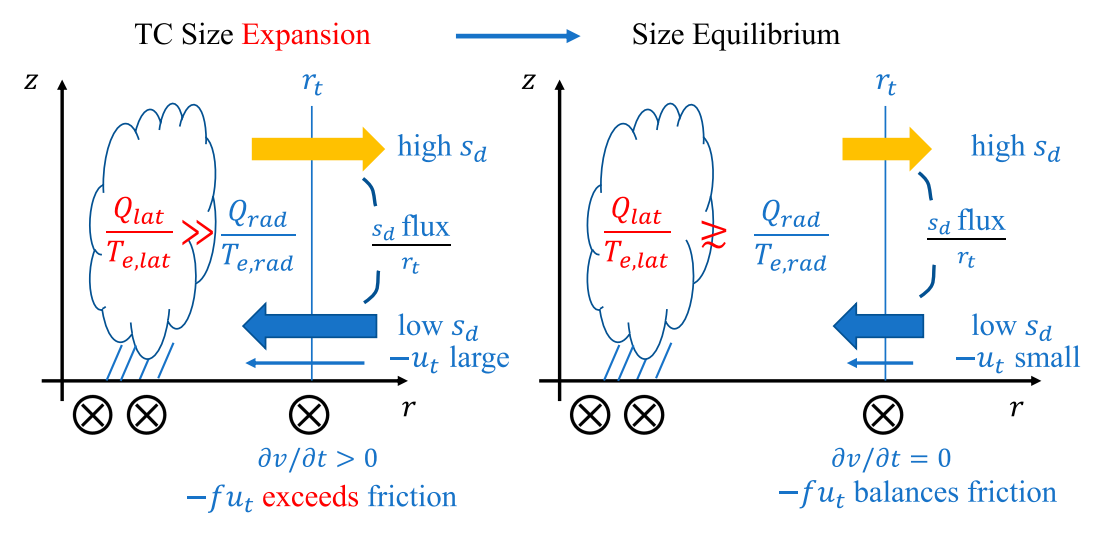


FIG. 1. A schematic plot of the expansion model presented in section 2. See the text for details.

Such a quantitative link, either direct or indirect, is necessary for a predictive model for size. Indeed, if given an inflow velocity, then size expansion may be predicted as shown in Wang and Toumi (2022). However, the inflow velocity varies significantly with height, from larger values within the boundary layer to near zero at some height above the top of the boundary layer. Thus, one needs to consider the integrated inflow mass flux instead of picking one single height.

In this study, we propose a model for size expansion toward equilibrium on the f plane, in terms of the outer radius of a certain tangential wind speed at the top of the boundary layer. We seek a model that

- is predictive and analytic;
- yields a characteristic expansion rate from the environmental/ external parameters;
- explains the physical process that drives TC expansion and why this expansion vanishes such that there exists an upper bound of size.

We test these model outcomes via comparison of model predictions with sets of numerical simulation experiments.

Our model for TC size expansion is presented in section 2. Basic predictions of the model and its comparison to numerical simulations are provided in sections 3–5. Further physical interpretations of the model are provided in section 6. A summary of key conclusions and discussion is given in section 7.

2. Theory: An analytical outer-size-expansion model on the f plane

a. Basic model structure

Below, we present a theory for TC expansion toward equilibrium that is summarized conceptually as follows: 1) in

radiative–convective equilibrium (RCE) without a TC, net condensational heating equals net radiative cooling; 2) when a TC forms, the TC volume is shifted substantially out of RCE, such that condensational heating substantially exceeds radiative cooling (consistent with enhanced surface fluxes); and 3) the TC expands in response as a result of strong low-level inflow as part of the overturning circulation that exports excess heat. As it expands, area-integrated radiative cooling increases faster than net condensational heating until low-level inflow is weak enough so that surface friction prevents any further expansion of wind field. The storm has reached its equilibrium size. A schematic plot is shown in Fig. 1.

We define r_t as the radius of a fixed tangential velocity v_t (e.g., r_8 is the radius of $v_t = 8 \text{ m s}^{-1}$ tangential wind) at the top of the boundary layer in the TC outer-core region. As TC size expansion is basically low-level spinup of TC outer core, the expansion rate of r_t can be given by

$$\frac{dr_t}{dt} = \frac{\partial v}{\partial t} / \left(-\frac{\partial v}{\partial r} \right), \quad r = r_t, \tag{1}$$

which is obtained by taking dv/dt = 0 with v = v[r(t), t], where v is the tangential wind, r is the radius, and t is the time. This relation is also presented in Tsuji et al. (2016).

The local spinup tendency for an axisymmetric TC at any height on the f plane is given by

$$\frac{\partial v}{\partial t} = -u(f + \zeta) - w \frac{\partial v}{\partial z} + F, \quad r = r_t, \tag{2}$$

where $\zeta = (\partial v/\partial r) + (v/r)$ is the relative vorticity, u is the radial velocity, w is the vertical velocity, and $F \approx (1/\rho_d)(\partial \tau_v/\partial z)$ is the

¹ For TC size, one may consider a single outer wind radius because the wind field structure is fully specified from a single input size (Chavas et al. 2015).

² Technically, r_t is understood as $r_t = r(v_t, t, \vartheta)$, where ϑ represents a series of environmental parameters and v_t is a time-independent tangential velocity. Since the main focus for the expansion rate is with a fixed v_t in a given environment (fixed ϑ), we write dr_t/dt instead of $\partial r_t/\partial t$.

turbulence frictional force, with ρ_d being the dry air density and τ_v being the turbulence stress in the azimuthal direction. Equation (2) is simplified by choosing r_t sufficiently far from the center so that ζ can be neglected compared to f. Further integrating Eq. (2) from the surface to h_w , some height in the lower troposphere below which the inward mass flux constitutes the majority of the total lateral inward mass flux, and neglecting vertical advection, gives

$$\frac{\partial v}{\partial t} \approx -fu_t - C_d(\mu v_t)^2 / h_w, \tag{3}$$

where the aerodynamic formula for surface stress $\tau_{v,sfc} = \rho_d C_d | V_{10} | v_{10}$ is applied, with C_d being the surface exchange coefficient for momentum, V_{10} being the 10-m surface horizontal velocity, and v_{10} being the 10-m tangential velocity, u_t is the vertical mean radial velocity, v_t is the corresponding tangential velocity at the top of the boundary layer at r_t , and μ is a surface wind reduction factor (i.e., basically the ratio of v_{10} to v_t). An implicit assumption made moving from Eq. (2) to (3) is that $\partial v/\partial t$ and ζ are approximately constant in the vertical below h_w .³ In Eq. (3), the second term on the RHS can be taken as a constant, a key conceptual benefit since we are following the radius of a fixed wind speed. Substituting Eq. (3) into Eq. (1) gives

$$\frac{dr_t}{dt} = \frac{1}{\left(-\frac{\partial v}{\partial r}\right)} \left[-fu_t - C_d(\mu v_t)^2 / h_w\right]. \tag{4}$$

There are two quantities $\partial v/\partial r$ and u_t that are not specified and must be linked to internal processes or environmental parameters. The slope of the wind profile $\partial v/\partial r$ can be obtained from the wind profile solution for the outer wind field from Emanuel (2004, hereafter E04) model (see appendix A), which depends only on the environmental parameters. The E04 model does not have a simple analytical solution, but we will provide an analytic approximation for $\partial v/\partial r$ based on this model in section 2b. An expression for u_t is derived next.

We propose u_t to be driven principally by the energetics of the TC, i.e., latent heating and radiative cooling, which can be described by a dry-entropy budget. Here, dry entropy is loosely defined by $s_d = c_p \ln(\theta/T_{\rm trip})$, where c_p is the specific heat of dry air at constant pressure, θ is the potential temperature, and $T_{\rm trip}$ is the triple-point temperature; s_d thus defined is a close approximation of the true dry entropy and is more convenient for budget analysis in numerical simulations. The budget of the dry entropy s_d within the TC volume from the center to r_t is written as

$$\frac{\partial S}{\partial t} = \frac{Q_{\text{lat}}}{T_{e,\text{lat}}} - \frac{Q_{\text{rad}}}{T_{e,\text{rad}}} + \dot{S}_{\text{res}} + \mathcal{F}_r + \mathcal{F}_u, \tag{5}$$

where S is the mass-integrated dry entropy within the volume; Q_{lat} and Q_{rad} are the net condensational heating (latent heat) and the total radiative cooling (defined positive), respectively, with $T_{e,lat}$ and $T_{e,rad}$ being their respective effective temperatures; \dot{S}_{res} represents other sources of dry entropy, such as surface sensible heating, diffusion of sensible heat, and dissipative heating; and \mathcal{F}_r and \mathcal{F}_u are the fluxes of dry entropy into the volume from the lateral (at r_t) and vertical directions (at the upper extent of the volume), respectively.⁴ The first two terms on the RHS are dry-entropy sources due to latent heating and radiative cooling, respectively. See appendix D for detailed expressions. To achieve a simple expression for size expansion, we neglect $\partial S/\partial t$, \dot{S}_{res} , \mathcal{F}_u . This assumes that the dominant terms are sources/sinks from latent heating (source), radiative cooling (sink), and net lateral transport into the TC from the environment (supported by simulations in appendix D). Doing so yields the balance equation

$$\frac{Q_{\text{lat}}}{T_{e,\text{lat}}} - \frac{Q_{\text{rad}}}{T_{e,\text{rad}}} \approx -\Delta s_d 2\pi r_t \rho_i u_t h_w, \tag{6}$$

where we have rewritten the lateral flux term in terms of a bulk free-tropospheric dry static stability given by

$$\Delta s_d = \mathcal{F}_r / (2\pi r_t \rho_i u_t h_w). \tag{7}$$

Though Δs_d must also depend on the vertical profile of lateral flow (for which we lack a clear constraint), the physical meaning of Δs_d can be better understood in the ideal case where the inflow is confined to near the surface and the outflow is confined to near the tropopause level: In this case, Δs_d represents the difference of s_d between the surface and tropopause. Appendix D shows that this is a reasonable assumption for TCs; discussion of the meaning of Δs_d in general is also provided in appendix D. The parameter ρ_i is an effective inflow air density corresponding to u_t so that $2\pi r_t \rho_i u_t h_w$ is the lateral mass flux at r_t below h_w . A reference of Δs_d is the difference between moist entropy and dry entropy near the sea surface, which is equivalent to the difference of s_d between tropopause and surface. A corresponding sufficient condition⁵ is the eyewall being in slantwise neutrality, which applies to the later stage of TC intensification and peak intensity (Bryan and Rotunno 2009; Peng et al. 2018; Wang et al. 2021b), which is the principal period for size expansion to occur (e.g., Martinez et al. 2020). For near-surface air with water vapor mixing ratio $q_v = 0.018 \text{ kg kg}^{-1}$, temperature T = 300 K, and relative humidity 80% (tropical value; see Dunion 2011), this gives a reference Δs_d of $L_{\nu}q_{\nu}/T \approx 150 \text{ J K}^{-1}\text{kg}^{-1}$, where $L_{\nu} = 2.501 \times 10^{-1} \text{ kg}^{-1}$ 106 J kg⁻¹ is the latent heating of vaporization. Thus, Δs_d can be taken as primarily determined by sea surface temperature.

³ A diagnostics of ensemble simulations of the CTL experiment (appendix C) shows that this assumption is generally reasonable except that it deviates more from simulations at the beginning stage of the expansion process, suggesting a potentially lower predictive capability of the expansion model at the beginning of stage of the TC size expansion.

⁴ A dry static energy budget is also viable, and the effective temperatures will not appear so that sensible and latent heat need not be separated. However, we use dry-entropy budget because it is more tractable for comparison with numerical simulations.

⁵ This specific assumption is common but is not critical to the present theory since it is a storm-integrated theory.

Latent heating is assumed to be principally produced in the eyewall (see appendix D), which is largely driven by boundary layer frictional convergence as found in both observations of vertical velocities (Stern et al. 2016) and implicit in the slantwise neutrality assumption of potential intensity theory (Emanuel 1986, 1995; Khairoutdinov and Emanuel 2013). Hence, Q_{lat} may be written as

$$Q_{\text{lat}} = \frac{\epsilon_{p,\text{ew}}}{\alpha_p} \ Q_{c,\text{ew}} \approx \frac{\epsilon_{p,\text{ew}}}{\alpha_p} \ L_v q_{vb} M_{\text{ew}}, \tag{8}$$

where q_{vb} is the boundary layer water vapor mixing ratio just outside of the eyewall corresponding to M_{ew} ; $\epsilon_{p,\mathrm{ew}}$ is the precipitation efficiency in the eyewall region, defined as the ratio of condensation to the mass of water vapor imported upward into the eyewall (see appendix D for practical diagnosis); $\mathcal{Q}_{c.ew}$ is the latent heating rate due to the total condensation in the eyewall; α_p is the ratio of net latent heating in the eyewall region to that within r_t ; and M_{ew} is the eyewall updraft mass flux. Given that the eyewall updraft is driven by boundary layer frictional convergence, $M_{\rm ew}$ is also equal to the friction-induced inflow mass flux into the eyewall. Thus, $M_{\rm ew}/\rho_{\rm w}$ (which will appear shortly) should be strongly controlled by the inner-core size and TC intensity, where ρ_w is the effective dry air density for the boundary layer inflow under the eyewall (close to ρ_i ; see appendix C for calculation). Here, ρ_w becomes implicit, as in the boundary layer momentum equations, only the gradient wind matters and air density will not explicitly appear (Kuo 1982; Kepert

The radiative cooling $\mathcal{Q}_{\mathrm{rad}}$ may be written as (Chavas and Emanuel 2014)

$$Q_{\rm rad} = \pi r_l^2 c_p \, \frac{\Delta p}{g} \, Q_{\rm cool}, \tag{9}$$

where

$$\Delta p = \frac{p_0}{R/c_p + 1} \left[\left(\frac{p_s}{p_0} \right)^{1 + R/c_p} - \left(\frac{p_t}{p_0} \right)^{1 + R/c_p} \right].$$

In the above, $Q_{\rm cool}$ is a constant radiative cooling rate for potential temperature, $\Delta p/g$ is the effective mass obtained by the vertical integration over a pressure layer, with g being the gravitational acceleration, $p_0=1000$ hPa is the reference pressure, R is the gas constant of dry air, and c_p is the heat content of dry air at constant pressure. Taking the surface pressure $p_s=1000$ hPa and the tropopause pressure $p_t=100$ hPa with $Q_{\rm cool}=1$ K day⁻¹ yields a value of 88 W m⁻², close to the 100 W m⁻² value in tropics (Pauluis et al. 2000).

An expression for the inflow velocity is obtained by first rearranging Eq. (6):

$$-u_{t} = \frac{1}{2\pi r_{t}h_{w}\rho_{i}} \left(\frac{Q_{\text{lat}}}{T_{e,\text{lat}}\Delta s_{d}} - \frac{Q_{\text{rad}}}{T_{e,\text{rad}}\Delta s_{d}} \right), \tag{10a}$$

and then substituting for \mathcal{Q}_{lat} using Eq. (8) and \mathcal{Q}_{rad} using Eq. (9) to yield

$$-u_{t} = \frac{1}{2\pi h_{w}} \frac{\epsilon_{p,\text{ew}}}{\alpha_{p}} \frac{L_{v}q_{\text{vb}}}{T_{e,\text{lat}}\Delta s_{d}} \left(\frac{M_{\text{ew}}}{\rho_{w}}\right) \frac{1}{r_{t}} - \frac{1}{2h_{w}} c_{p} \frac{\Delta p}{\rho_{i}g} \frac{Q_{\text{cool}}}{T_{e,\text{rad}}\Delta s_{d}} r_{t},$$

$$(10b)$$

where we take $\rho_i \approx \rho_w$. We may write this more compactly as

$$-u_{t} = \frac{1}{h_{w}} A \left(\frac{M_{\text{ew}}}{\rho_{w}} \right) \frac{1}{r_{t}} - \frac{1}{h_{w}} B r_{t}, \tag{10c}$$

where we define two thermodynamic parameters

$$A = \frac{1}{2\pi} \frac{\epsilon_{p,\text{ew}}}{\alpha_p} \frac{L_v q_{\text{vb}}}{T_{e,\text{lat}} \Delta s_d} \quad \text{and}$$
 (11a)

$$B = \frac{1}{2} c_p \frac{\Delta p}{\rho_i g} \frac{Q_{\text{cool}}}{T_{e,\text{rad}} \Delta s_d}.$$
 (11b)

Parameter A is nondimensional and is related to the latent heating that drives expansion, while B is a velocity and is related to radiative cooling that suppresses expansion.

The size-expansion model is obtained by substituting Eq. (10c) into Eq. (4) to yield

$$\frac{dr_t}{dt} = \frac{r_{t,\text{eq}} - r_t}{\tau_{\text{rt}}}.$$
 (12)

Here, $r_{t,eq}$ is the equilibrium size when $dr_t/dt = 0$ is achieved [Eq. (12)] and τ_{rt} is the time scale for expansion. Equation (12) states that the expansion rate is given by the difference in size from equilibrium divided by a time scale τ_{rt} .

Quantity $r_{t,eq}$ in Eq. (12) is given by

$$r_{t,\text{eq}} = \left[fA \left(\frac{M_{\text{ew}}}{\rho_w r_t} \right) - C_d (\mu \nu_t)^2 \right] / (fB), \tag{13a}$$

which can be expressed explicitly by Q_{lat} and Q_{cool} as [using Eqs. (8) and (11)]

$$r_{t,\text{eq}} = \left[f \frac{1}{2\pi r_t \rho_i} \frac{Q_{\text{lat}}}{T_{e,\text{lat}} \Delta s_d} - C_d (\mu \nu_t)^2 \right] / \left[\frac{1}{2} f c_p \frac{\Delta p}{\rho_i g} \frac{Q_{\text{cool}}}{T_{e,\text{rad}} \Delta s_d} \right]. \tag{13b}$$

Equations (13a) and (13b) indicate that $r_{t,eq}$ may vary with r_t (and thus time), but here, we will take it to be a constant in order to seek an analytical solution of Eq. (12); this assumption is later tested in section 4b. A useful form of $r_{t,eq}$ is obtained by writing Eq. (13a) at equilibrium ($r_t = r_{t,eq}$):

$$r_{t,\text{eq}} = \left[f A \left(\frac{M_{\text{ew}}}{\rho_w} \right)_{\text{eq}} \frac{1}{r_{t,\text{eq}}} - C_d (\mu \nu_t)^2 \right] / (Bf), \tag{14}$$

where the subscript "eq" means equilibrium. Before solving for $r_{t,eq}$, we first define the equilibrium radius of zero net source of dry entropy $r_{RCE,eq}$, inside of which the system is in RCE, by taking the LHS of Eq. (6) to be zero [using Eqs. (8) and (9)] and solving for r_t at equilibrium:

$$r_{\text{RCE,eq}} = \sqrt{\frac{A}{B} \left(\frac{M_{\text{ew}}}{\rho_w} \right)_{\text{eq}}}$$
 (15)

Thus, $r_{\rm RCE,eq}$ scales with $\sqrt{(M_{\rm ew}/\rho_w)_{\rm eq}}$ (this relationship will be revisited later). Note that $r_{\rm RCE,eq}$ cannot be obtained by directly taking $v_t=0$ in Eq. (14) because $v_t=0$ implies $u_t=0$ in equilibrium [Eq. (4)], but Eq. (7) does not allow $u_t=0$. Substituting Eq. (15) into Eq. (14) and solving for $r_{t,\rm eq}$, we have

$$r_{t,\text{eq}} = \frac{-C_d(\mu v_t)^2 \frac{1}{Bf} + \sqrt{C_d^2(\mu v_t)^4 \frac{1}{B^2 f^2} + 4r_{\text{RCE,eq}}^2}}{2}, \quad (16a)$$

which can be written compactly as

$$r_{t,\text{eq}} = \frac{-\xi v_t^2 + \sqrt{\xi^2 v_t^4 + 4r_{\text{RCE},\text{eq}}^2}}{2}$$
 (16b)

by defining

$$\xi = C_d \, \frac{\mu^2}{Bf}.\tag{17}$$

Equations (16a) and (16b) imply that $r_{t,eq}$ scales with 1/f if $r_{RCE,eq}$ scales with 1/f. Equation (16b) also shows that $r_{RCE,eq} > r_{t,eq}$. The time scale for expansion τ_{rt} in Eq. (12) is given by

$$\tau_{\rm rt} = \left(-\frac{\partial v}{\partial r} \right) \frac{h_w}{fR} \,. \tag{18}$$

Here, $\tau_{\rm rt}$ is proportional to 1/f and $\partial v/\partial r$, meaning that the time scale is larger if f is smaller or the local slope of the wind profile is larger in magnitude. Note that $\tau_{\rm rt}$ exists independent of the specific parameters for eyewall dynamics, as it depends on B but not A.

Conceptually, the model links the expansion to the radial velocity u_t induced by the dry-entropy imbalance within the TC volume. A stable equilibrium size $r_{t,\rm eq}$ independent of time and current size is assumed to exist [Eq. (12)]. The following parameters of the model are taken as constants: $\epsilon_{p,\rm ew}$, α_p , h_w , f, L_v , q_{vb} , $T_{e,\rm lat}$, $T_{e,\rm rad}$, Δs_d , Δp , and ρ_i , and thus A, B, and ξ . Doing so simplifies the problem enough to make it analytically tractable. Simulations also indicate that taking parameters $\epsilon_{p,\rm ew}$, α_p , Δs_d , Δp (implicit in Fig. D1), ρ_i (not shown, also $T_{e,\rm lat}$ and $T_{e,\rm rad}$) as constant is reasonable (see appendix D). Note a constant $r_{t,\rm eq}$ also implies a constant $M_{\rm ew}/(\rho_w r_t)$ [Eq. (13a)]. In this manner, $\mathcal{Q}_{\rm lat}$ is proportional to r_t [Eq. (8)] and $\mathcal{Q}_{\rm rad}$ is proportional to r_t^2 [Eq. (9)]. Hence, u_t [Eq. (10)]

monotonically decreases in magnitude with expansion so that TC size will approach an equilibrium.

If, in addition to $r_{t,eq}$, τ_{rt} is also time invariant, the solution of Eq. (12) with initial condition $r_t(t_0) = r_{t0}$ is given by

$$r_t(t) = (r_{t0} - r_{t,eq})e^{-(t-t_0)/\tau_{rt}} + r_{t,eq}.$$
 (19)

As $\tau_{\rm rt}$ is positive definite, r_t will exponentially approach the equilibrium size $r_{t,\rm eq}$, where $\tau_{\rm rt}$ is the e-folding time scale. Moreover, $r_{t,\rm eq}$ is a stable equilibrium, as size approaches $r_{t,\rm eq}$ for $r_{t0} < r_{t,\rm eq}$ (expansion) and $r_{t0} > r_{t,\rm eq}$ (shrinking). Equation (19) gives an exponential solution, similar to Wang and Toumi (2022) for absolute size, though this solution is exponential in the decay of the distance from equilibrium and hence allows for size to reach an equilibrium value as is known to exist on the f plane.

Up to this point, $\partial v/\partial r$ in τ_{rt} [Eq. (18)] is not yet defined analytically, which is needed for a full analytical solution of Eq. (12). Moreover, $r_{t,eq}$ [Eq. (13)] is not yet defined in terms of environmental parameters, which requires an expression for $(M_{ew}/\rho_w)_{eq}$. In the following subsections, we will resolve these issues and obtain a full analytical solution of Eq. (12).

b. Analytical expression of ∂υ/∂r

Equation (16) provides an expression for the equilibrium radii of different wind speeds, which has the exact same form as the E04 model (see appendix A). The slope of the equilibrium wind profile $\partial v_t \partial r_{t,eq}$ can be obtained by taking the derivative of $r_{t,eq}$ with respect to v_t in Eq. (16) in a fixed environment:

$$\left(\frac{\partial v_t}{\partial r_{t,\text{eq}}}\right)^{-1} = \frac{\partial r_{t,\text{eq}}}{\partial v_t} = -\frac{2v_t \left(\frac{1}{2}v_t \xi' + \xi\right) r_{t,\text{eq}}}{2r_{t,\text{eq}} + \xi v_t^2},\tag{20}$$

where $\xi' = d\xi/dv_t$. Equation (20) has the same form as the E04 model (see appendix A). Note that ξ is a constant with respect to r_t in a given environment when v_t is fixed but may vary with v_t . For example, closer to the center (larger v_t), the absolute vorticity is larger, so ξ should decrease accordingly (though above we have approximated the absolute vorticity by f). Here, as ξ' should also be a constant with respect to r_t at fixed v_t to simplify the math, we take the approximation $(1/2)v_t\xi' + \xi = \sigma\xi$, with σ being a constant fitting parameter. Here, σ is set to a constant value of 0.7 (for $v_t = 8 \text{ m s}^{-1}$, shown below).8 Note that $\sigma > 0$ is presumed so that the RHS of Eq. (20) is negative, corresponding to a TC wind profile in which the azimuthal wind speed decreases with radius.

⁶ Actually, $r_{\text{RCE,eq}}$ would be equivalent to $r_{0,\text{eq}}$, the equilibrium radius of vanishing wind, if $\lim_{v_t \to 0} \xi v_t^2 = 0$. A close relation between $r_{\text{RCE,eq}}$ and $r_{0,\text{eq}}$ is indeed seen in numerical experiments (not shown).

⁷ Diagnosed q_{vb} from the CTL simulation (appendix C) increases ~15% during expansion (not shown), but this size dependence is secondary because the expansion model eventually depends on equilibrium size $r_{t,eq}$. Note also that the q_{vb} increase is not explained by a corresponding surface pressure drop, which is only ~2.5%.

 $^{^8}$ Fitting parameter σ accounts for $d \ln \xi/d \ln v_t = -d \ln (\zeta + f)/d \ln v_t + d \ln (C_d \mu^2/B)/d \ln v_t = -d \ln \zeta_a/d \ln v_t + d \ln (C_d \mu^2/B)/d \ln v_t = 2(\sigma-1).$ Note f is originally ζ_a in Eq. (2); if $\zeta_a \approx f$ were not applied, the derivation up to Eq. (18) will be the same except replacing f by ζ_a . For $\partial v/\partial r$, ζ_a cannot be approximated by f as in Eq. (3); ζ must be retained here for a proper understanding. Qualitatively, ζ_a increasing with v is generally supported by the E04 solution. Quantitatively, $d \ln \zeta_a/d \ln v_t$ at r_8 is found in the E04 solution to generally increase from 0.2 to 0.4 with decreasing r_8 when $r_8 < 1000$ km and about 0.1 when $r_8 > 2000$ km (not shown). This translates to σ ranging from 0.8 to 0.95. The deviation from 0.7 should be accounted for by the assumptions made in Eq. (3) and by $d \ln (C_d \mu^2/B)/d \ln v_b$, which the present model cannot predict.

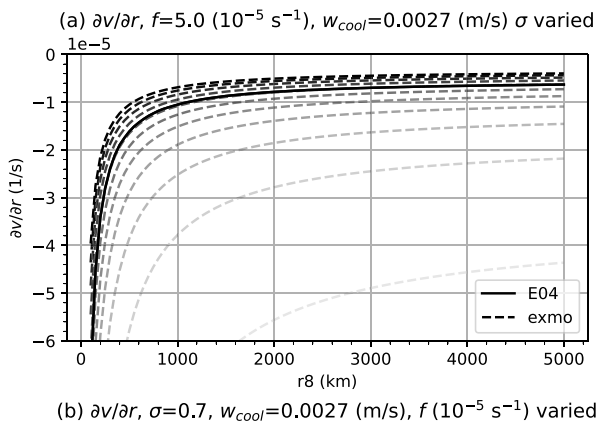
With this, we rewrite Eq. (20) in general by dropping the subscript "eq" and write ξ as ξ_0 to mark that it is only associated with $\partial \upsilon / \partial r$.

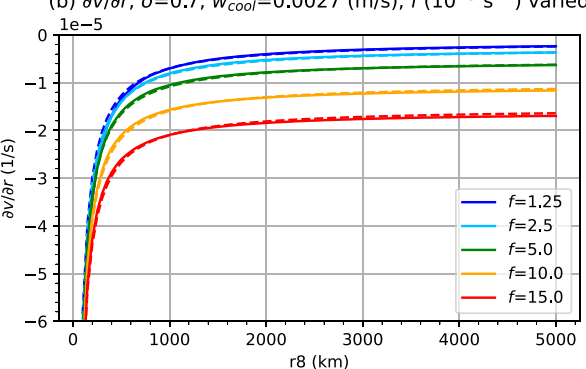
$$\left. \left(\frac{\partial v}{\partial r} \right)^{-1} \right|_{v=v_{\star}} = \frac{\partial r}{\partial v} \bigg|_{v=v_{\star}} = -\frac{2r_{t}v_{t}\sigma\xi_{0}}{2r_{t} + \xi_{0}v_{t}^{2}}.$$
 (21)

The assumption implicitly made to move from Eqs. (20) to (21) is that $(\partial v/\partial r)|_{v=v_t}$ at given r_t and v_t for slowly evolving wind fields can be approximated by equilibrium values. This assumption follows the fairly nice performance of the E04 model, which is derived for steady state, of matching observed TC outer wind profiles for storms that are not necessarily in steady state (Chavas et al. 2015). This assumption will be shown to work nicely in section 5. Equation (21) provides an analytical approximation of $\partial v/\partial r$. Compared to the full E04 model, Eq. (21) does not need numerical integration but still contains similar physics to the E04 model. Additional discussion of the properties of Eq. (21) is provided in appendix B. In the next subsection, we will substitute Eq. (21) into Eq. (18) to yield an analytical solution of Eq. (12).

Now, we demonstrate that $\sigma=0.7$ is useful for $\partial\upsilon/\partial r$ [Eq. (21)] at $\upsilon_t=8~{\rm m~s^{-1}}$ (this specific υ_t will be used for the evaluation of the model in sections 3 and 4). We define a baseline environment of $\xi_0=35\,105~{\rm s^2~m^{-1}}$ with $f=5\times10^{-5}~{\rm s^{-1}}$, $C_d=0.0015$, and surface air temperature $T_s=300~{\rm K}$ for demonstration (note that a complete parameter setting in this baseline environment is given in section 3). The radiative-cooling-induced subsidence velocity $w_{\rm cool}=0.0027~{\rm m~s^{-1}}$ is set (positive downward) for the E04 model in the baseline environment. The quantity $\partial\upsilon/\partial r$ at r_8 from the E04 model (solid) and in Eq. (21) (dashed) in the baseline environment is shown in Fig. 2a. The parameter σ is varied from 0.1 to 1.1 to show the sensitivity of Eq. (21) to this quantity. Indeed, Eq. (21) with $\sigma=0.7$ does very well in reproducing $\partial\upsilon/\partial r$ for any value of r_8 and over a wide range of values of f (Fig. 2b), compared to the E04 model.

In addition, we test whether Eq. (21) performs reasonably when $w_{\rm cool}$ changes. Note the present expansion model is not framed to have $w_{\rm cool}$ but have B playing the same role in Eq. (21) as $(1/2)w_{\rm cool}$ in the E04 model (see appendix A). In addition, as $w_{\rm cool} \approx Q_{\rm cool}/(\partial\theta/\partial z)$ and $\partial\theta/\partial z$ can be considered mainly determined by sea surface temperature $T_{\rm SST}$, thus $w_{\rm cool}$ may be considered as a function of $Q_{\rm cool}$ and $T_{\rm SST}$, both of which enters Eq. (21) through ξ_0 by B [Eq. (11b)]. To vary $w_{\rm cool}$, we pick four values 0.0042, 0.0032, 0.0027, and 0.0022 m s⁻¹ for the E04 model, which corresponds to $T_{\rm SST}=286$, 293, 300, and 307 K, 9 respectively, in the set of numerical experiments sea





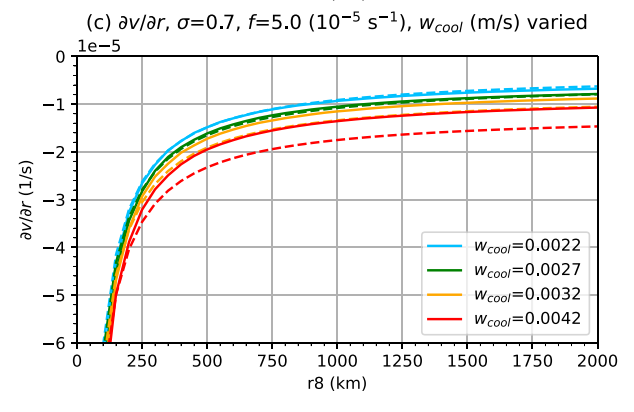


FIG. 2. (a) The value $\partial v/\partial r$ at r_8 from the E04 model (solid) and the expansion model Eq. (21) (dashed) with σ varied from 0.1 to 1.1 (light to dark, with an interval of 0.1) at $f=5\times 10^{-5}~\rm s^{-1}$ and $w_{\rm cool}=0.0027~\rm m~s^{-1}$. (b) As in (a), but with $\sigma=0.7$ and with different $f(10^{-5}~\rm s^{-1}$; see the legend); the E04 model in solid lines and Eq. (21) in dashed lines. (c) As in (b), but for different $w_{\rm cool}$ (m s⁻¹; see the legend) for the E04 model (solid) and $T_{\rm SST}$ (286, 293, 300, 307 K; warmer color means lower $T_{\rm SST}$) for Eq. (21) (dashed). See the text for parameter settings.

surface temperature $T_{\rm SST}$ (ExSST) (see appendix C), for Eq. (21). Quantity $Q_{\rm cool}=1$ K day $^{-1}$ is set. The $\partial v/\partial r$ at r_8 is shown in Fig. 2c. It is seen that Eq. (21) works qualitatively the same as the E04 model: Higher SST corresponds to lower magnitude of slope, except that Eq. (21) produces a larger variation of $\partial v/\partial r$ than the E04 model. This is associated with the fact that B basically follows with the Clausius–Clapeyron (C–C) scaling while $w_{\rm cool}$ appears to vary more

⁹ The corresponding *B* is 0.0016, 0.0011, 0.0007, 0.0005 m s⁻¹, about half of $(1/2)w_{cool}$. This quantitative difference by itself does not indicate that Eq. (21) is wrong; rather, it raises a question whether the E04 model is correct as a result of compensating errors. As shown in appendix A, the E04 model is a mass-balance derivation in the same framework as for Eq. (21), which is an energy (entropy)-balance derivation. As both are physical, the error should arise from simplifying assumptions. For the E04 model, the uncertainty seems to be whether the actual subsidence velocity is indeed a radially constant value given by w_{cool} . However, an analysis toward a more complete mechanistic understanding of $\partial v/\partial r$ is out of the scope of this study.

slowly. It will be shown in section 5 that Eq. (21) turns out to match nicely with simulations.

As discussed above and demonstrated by Fig. 2, we use Eq. (21) with $\sigma = 0.7$ for $(\partial v/\partial r)|_{v=v}$ in the expansion model.

Combining Eqs. (18) and (21) gives a final expression for $\tau_{\rm rt}$:

$$\tau_{\rm rt} = \frac{2r_t + \xi_0 v_t^2 h_w}{2r_t v_t \sigma \xi_0} \frac{h_w}{fB}.$$
 (22)

c. Analytical solution for size evolution

Substituting Eq. (22) into Eq. (12) yields

$$\frac{dr_t}{dt} = 2 \frac{fB}{h_w} \sigma \xi_0 v_t \frac{r_t (r_{t,eq} - r_t)}{2r_t + \xi_0 v_t^2},$$
(23)

which gives an explicit form of the expansion rate $(dr_t/dt > 0)$ when $0 < r_t < r_{t,eq}$ and $dr_t/dt < 0$ when $r_t > r_{t,eq}$). Equation (23) again indicates that $r_{t,eq}$ is a stable equilibrium, and $dr_t/dt = 0$ when $r_t = r_{t,eq}$ (and for $r_t = 0$). The maximum expansion rate occurs at a size given by

$$r_{t,\text{expmax}} = \frac{-\xi_0 v_t^2 + \sqrt{\xi_0^2 v_t^4 + 2r_{t,\text{eq}} \xi_0 v_t^2}}{2},$$
 (24)

where it is seen $0 < r_{t,expmax} < r_{t,eq}/2$. When $r_t > r_{t,eq}$, $(\partial/\partial r_t)(dr_t/dt) < 0$, meaning that size shrinks faster toward $r_{t,eq}$ when r_t is farther from $r_{t,eq}$.

Solving Eq. (23) with the initial condition $r_t = r_{t0}$ at $t = t_0$ gives

$$t - t_0 = \frac{1}{2\xi_0 v_t \frac{fB\sigma}{h}} \left[-\left(2 + \frac{\xi_0 v_t^2}{r_{t,eq}}\right) \ln \left(\frac{r_{t,eq} - r_t}{r_{t,eq}} - r_{t0}\right) + \frac{\xi_0 v_t^2}{r_{t,eq}} \ln \left(\frac{r_t}{r_{t0}}\right) \right], \quad r_t > 0 \quad \text{and} \quad r_t \neq r_{t,eq}.$$
 (25)

Equation (25) is the analytical solution of the full size-expansion model in section 2a. The solution is expressed by time t as a function of r_t , which is an implicit function of t; an analytic solution for $r_t(t)$ is not tractable. The input parameters are all external or environmentally defined (presently $r_{t,eq}$ can be either external or environmentally defined by TC PS). A method for determining $r_{t,eq}$ [Eq. (16b)] from environmental parameters is provided next.

d. Formulation for updraft mass flux

An environmentally defined $r_{t,eq}$ will be obtained through Eqs. (15) and (16b) if $(M_{ew}/\rho_w)_{eq}$ is environmentally defined. In this subsection, we parameterize $(M_{ew}/\rho_w)_{eq}$ by using a combination of theory and empirical estimation based on numerical simulation results.

The parameterization may be derived directly from mass continuity: The eyewall updraft mass flux is balanced by a constant subsidence velocity, which is usually assumed to be driven by radiative cooling (e.g., E04). The streamfunction is given by $\partial \psi / \partial r = 2\pi \rho_d r w$, where ρ_d is the dry air density and w is the vertical velocity. Integrating radially over the subsidence region at the altitude of h_w yields

$$r_{\psi_0}^2 \approx \frac{\psi_{\text{max}}}{\pi \rho_w w_{\text{cool}}} + r_{\psi_{\text{max}}}^2,$$
 (26)

where $r_{\psi 0}$ and $r_{\psi max}$ are the radii of $\psi=0$ and maximum ψ (or ψ_{max}) at h_w , respectively, and w_{cool} is the environmental clearair subsidence velocity (positive downward). The inner radius term $r_{\psi_{max}}^2$ may be neglected as it is more than an order of magnitude smaller than $r_{\psi_0}^2$. Hence,

$$\psi_{\text{max}} \approx \pi \rho_w w_{\text{cool}} r_0^2, \tag{27}$$

where r_0 , the radius of vanishing wind, should be equivalent to $r_{\psi 0}$ in E04. TC PS shows that equilibrium r_0 (or $r_{0,eq}$) scales

with $V_{\rm Carnot}/f$, which does not depend on C_d . Following our assumption that most of the upward mass flux occurs within the eyewall so that $M_{\rm ew} \approx \psi_{\rm max}$, thus, we propose that

$$\sqrt{(M_{\rm ew}/\rho_w)_{\rm eq}} \propto \sqrt{\pi w_{\rm cool}} C_d^{\nu} V_{\rm Carnot}/f$$
 (28),

a relationship we test with numerical simulations, with ν being a constant coefficient. Here, a role of C_d is tested as it may influence the eyewall upward mass flux by influencing surface friction. Following Eq. (27) of Wang et al. (2022), $V_{\rm Carnot}$ is defined as

$$V_{\text{Carnot}}^2 = (\eta \epsilon_C L_v - R_v T_{\text{SST}}) q_{\text{vs}}^*, \tag{29}$$

where $\epsilon_C = (T_{\rm SST} - T_{\rm tpp})/T_{\rm SST}$ is the Carnot efficiency, $T_{\rm tpp}$ is the tropopause temperature, R_v is the gas constant of water vapor, $q_{\rm vs}^*$ is the saturation water vapor mixing ratio at $T_{\rm SST}$, and $\eta = 0.4$ is a coefficient accounting for the "triangle" shape of the thermodynamic cycle following section 3b of Wang et al. (2022).

The exact relationship is not known, and thus, we seek the relation in Eq. (28) via linear regression from equilibrium states of simulated TCs (see appendix C). There is a tight linear relationship between the two quantities in Eq. (28). We estimate the coefficient based on the linear fit to the experiment sets varying $T_{\rm tpp}$, C_d , C_k , and $T_{\rm SST}$ to avoid overfitting to the experiments varying f, whose slope deviates slightly, but the result holds reasonably well for those experiments too. The result is shown in Fig. 3. A best-fit estimate of $\nu = -0.07$ is obtained, which suggests that C_d has nearly zero effect on $(M_{\rm ew}/\rho_w)_{\rm eq}$, consistent with the finding in Wang et al. (2022). As a final result of the fitting, we have

$$\sqrt{\left(\frac{M_{\text{ew}}}{\rho_w}\right)_{\text{eq}}} = 0.79\sqrt{\pi w_{\text{cool}}} C_d^{-0.07} V_{\text{Carnot}} / f. \tag{30}$$

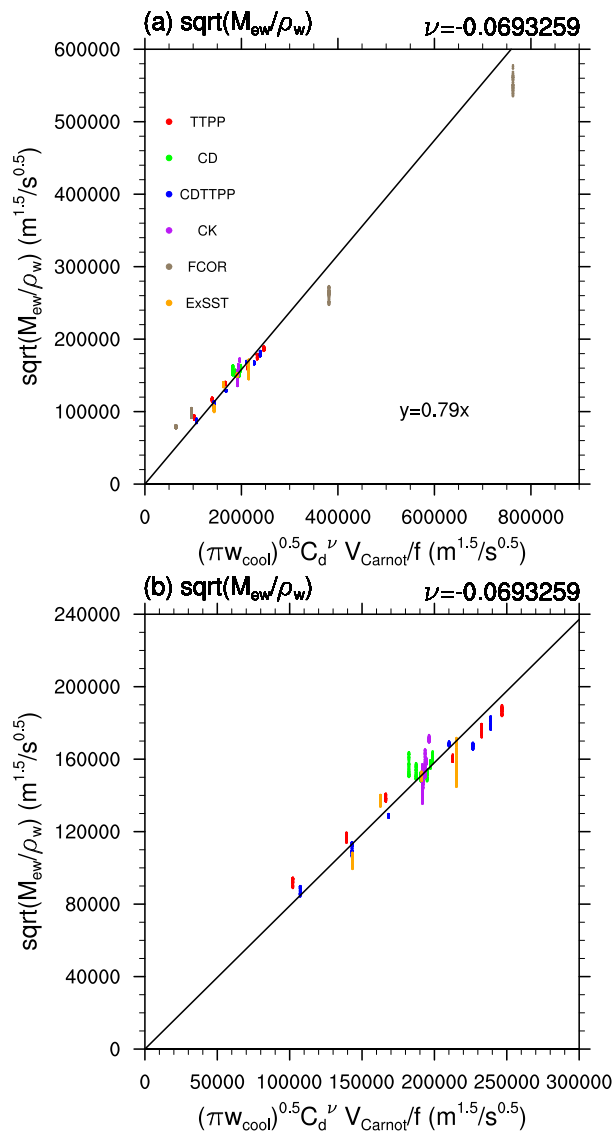


FIG. 3. (a) The term $\sqrt{(M_{\rm ew}/\rho_w)_{\rm eq}}$ (m^{1.5} s^{-0.5}) as a function of $\sqrt{\pi w_{\rm cool}} C_d^\nu V_{\rm Carnot}/f$ (m^{1.5} s^{-0.5}) in TTPP (red), CD (green), CDTTPP (blue), CK (purple), FCOR (gray), and ExSST (orange) during equilibrium periods. Data of TTPP, CD, CDTTPP, CK, and ExSST are used to determine ν by linear regression. Note that only ensemble index 0 in TTPP and ExSST is used, to be consistent with the sample sizes of CD, CDTTPP, and CK, which do not contain ensemble experiments. Fitted ν is shown on the upper right of the plot. Data are first processed by a 120-h running average. The black line visualizes the equation shown in the figure. In the equation, $y = \sqrt{(M_{\rm ew}/\rho_w)_{\rm eq}}$ and $x = \sqrt{\pi w_{\rm cool}} C_d^\nu V_{\rm Carnot}/f$. See appendix C for experimental design. (b) As in (a), but zoomed in without FCOR. Equilibrium periods for TTPP, FCOR, and ExSST are defined in section 4, and those for CD, CDTTPP, and CK are the same as TTPP.

The environmentally defined $r_{t,eq}$ is obtained by substituting Eq. (30) into Eq. (15) and substituting the resulting $r_{RCE,eq}$ into Eq. (16b). As discussed in section 2b, $r_{t,eq}$ will scale with 1/f and additionally increase with $C_d^{-0.07}V_{Carnot}$. The

expansion model is now capable of being fully predictive and analytic.

e. Model summary and implementation

To summarize, this section has proposed a model for the expansion of TC size in which expansion is driven by latent heating, which is dominated by heating in the eyewall and suppressed by radiative cooling. The model can be fully predictive and analytic if there is an environmentally defined size-independent $r_{t,eq}$. The steps to put the model into practice are as follows:

- Assuming known $r_{t,eq}$, the evolution of outer radius r_t is given by Eq. (25). Parameter B is given in Eq. (11b), and parameter $\xi_0 = \xi$ is given in Eq. (17). For $v_t = 8$ m s⁻¹, $\xi_0 = 35\,105$ s² m⁻¹ for $C_d = 0.0015$, $T_{SST} = 300$ K and $f = 5 \times 10^{-5}$ s⁻¹ and $\sigma = 0.7$.
- The equilibrium size $rt_{,eq}$ is predicted from the environmental parameters by using Eq. (30) $for(M_{ew}/\rho_w)_{eq}$, plugging the result into Eq. (15) to calculate $r_{RCE,eq}$ and plugging the result into Eq. (16) $for r_{t,eq}$.

Once given $r_{t,eq}$, Q_{lat} as a proportional function of r_t is calculated through Eqs. (15), (16), and (8), or directly by Eq. (13b). The radial velocity u_t is given by Eq. (10); the local tangential wind acceleration $\partial v/\partial t$ (at $r = r_t$) is given by Eq. (3).

In section 3, we examine the basic properties of the analytical solution for the evolution of storm size as well as the underlying physical processes of the model. In section 4, we use numerical simulations to test the model predictions of both expansion rate (section 4a) and $r_{t,eq}$ (section 4b). Section 5 provides detailed tests of the expansion model against numerical simulations in terms of simplifying assumptions and prediction of intermediate variables. Section 6a explores the physical meaning of $r_{t,eq}$. Section 6b examines the model's representation of the dependence of the inflow velocity, the local tangential wind spinup, and the size-expansion rate on the latent heating rate. Section 6c discusses the sensitivity of the model to Δs_d and other parameters.

3. Behavior of theoretical model

a. Parameter settings in baseline environment

We next discuss the basic behavior of the expansion model solution in an idealized baseline environment. We take $v_t = 8 \text{ m s}^{-1}$ as our outer-size wind speed, and hence we use r_8 in lieu of r_t at times. We define an idealized baseline environment for analysis with parameter values representative of tropical cyclones in the present-day tropical atmosphere. We set as constants: $f = 5 \times 10^{-5} \text{ s}^{-1}$; $Q_{\text{cool}} = 1 \text{ K day}^{-1}$; $h_w = 2.5 \text{ km}$ (depth that captures the majority of the lateral inflow mass flux); $\rho_i = 1.1 \text{ kg m}^{-3}$; $C_d = C_k = 0.0015$; $\mu = 0.92$ (to match CM1 simulations, where a surface gustiness has been added, described in appendix C); $L_v = 2.501 \times 10^6 \text{ J kg}^{-1}$; $\epsilon_{p,\text{ew}} = 1$, $\alpha_p = 0.8$ (indicating that the eyewall dominates the net latent heating in a TC, estimated from simulations in appendix C); and $\sigma = 0.7$. V_{Carnot} [Eq. (29)] is defined with $T_{\text{SST}} = 300 \text{ K}$, $T_{\text{tpp}} = 200 \text{ K}$, and environmental surface

pressure $p_s=1015$ hPa, which collectively yields $V_{\rm Carnot}=66~{\rm m~s}^{-1}$. These values correspond to the Control (CTL) simulation. We further set $q_{vb}=q_{vs}^*=0.022~{\rm kg~kg}^{-1}$, with q_{vs}^* being the environmental saturation mixing ratio of the surface air temperature. The parameter Δs_d is set to $\Delta s_d=L_vq_{vs}^*/T_s=187.1~{\rm J~K}^{-1}~{\rm Kg}^{-1}$, and we set $T_{e,{\rm rad}}=T_{e,{\rm lat}}=T_s$ without loss of generality. Tropopause pressure p_t is set to 100 hPa [for $Q_{\rm rad}$, Eq. (9), which gives 89.3 W m⁻²]. These settings yield A=0.16, $B=0.0007~{\rm m~s}^{-1}$, and $\xi=35\,105~{\rm s}^2~{\rm m}^{-1}$, and we set $\xi_0\equiv\xi$ throughout, except in section 6c. Finally, we set $w_{\rm cool}=0.0027~{\rm m~s}^{-1}$, which will only be used to calculate $r_{t,{\rm eq}}$ from $(M_{\rm ew}/\rho_w)_{\rm ew}$ [Eq. (30)] in section 4b. Unless otherwise noted, these values are held constant throughout so that the use of the analytic model is in as simple a setup as possible.

These constants are complete for the fully predictive size-expansion model and will be used for tests below unless otherwise noted. In particular, we will at times arbitrarily set $r_{t,eq}$ for certain examinations in sections 3–6, which will also be noted.

b. Behavior of theoretical model

In this subsection, we examine the basic behavior of our TC size-evolution model and the underlying physical processes.

First, the basic evolution of size predicted from our model [Eq. (25)] is shown in Fig. 4. Two representative cases are shown from an initial size of $r_{t0} = 250$ km at the initial time $t_0 = 0$ day: expansion toward a larger equilibrium size of $r_{t,eq} = 1200$ km (blue curve) and shrinking toward a smaller equilibrium size of $r_{t,eq} = 100$ km (red curve). For both cases, the model predicts a reasonable time scale of 10–20 days. The rate of expansion/shrinking vanishes as size approaches its equilibrium ($r_{t,eq}$). The maximum expansion rate occurs during the first half of the expansion process at a radius $r_{t,expmax}$ of approximately 500 km [Eq. (24)].

Next, we show the solution for expansion toward a range of equilibrium sizes $(r_{t,eq})$. The size evolution $r_t(t)$, expansion rate dr/dt, and time scale τ_{rt} are shown in Fig. 5. The radius r_8 increases with time and approaches $r_{t,eq}$ after day 20. Larger expansion rate corresponds to larger $r_{t,eq}$ (Fig. 5b). This is because the time scale τ_{rt} is the same across all experiments [Eqs. (12), (18), and (21), Fig. 5c], as this quantity is a function of size alone in this example. Time scale τ_{rt} monotonically decreases with size, with a first rapid decrease when $r_8 < 500$ km

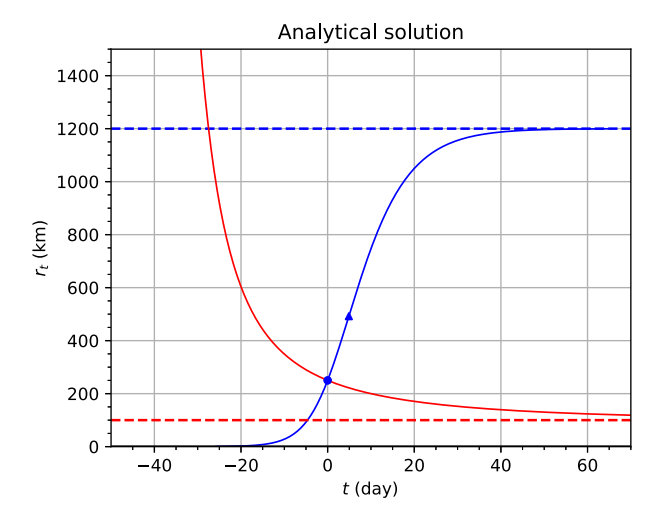


FIG. 4. Analytical solution of size evolution (r_t , km vs t, day; solid lines) in Eq. (25) for two cases: r_t expanding toward a larger $r_{t,eq}$ (blue) and r_t shrinking toward a smaller $r_{t,eq}$ (red). Horizontal dashed lines mark $r_{t,eq}$. Dots mark the initial condition t_0 and $r_{t,0}$. The triangle marks the location ($r_{t,expmax}$) of the maximum expansion rate

and slowly decrease afterward (note $\tau_{\rm rt} = 22.4$, 13.2, 10.2, 7.9 days at $r_8 = 250$, 500, 750, 1200 km, respectively, Fig. 5c). Physically, this is because the E04 model is flatter (smaller slope) for larger storm (longer tail) so from Eq. (18) $\tau_{\rm rt}$ becomes smaller too. Note that $\tau_{\rm rt}$ is greater than 15 days when the TC is small ($r_8 \approx 400$ km) and decreases below 10 days as size approaches $r_{t,\rm eq}$. The variation of $\tau_{\rm rt}$ is determined by the variation of $\partial v/\partial r$ at r_8 [Eq. (18), Fig. 2). Correspondingly, the expansion rate peaks at tens of kilometers per day (Fig. 5b), a similar order of magnitude to that seen in observations (Schenkel et al. 2023). Finally, the radius of the maximum expansion rate increases with $r_{t,\rm eq}$, following Eq. (24).

We next explore physically why the TC expands in the first place and why it eventually reaches equilibrium, following the conceptual diagram in Fig. 1. We examine the budget terms in the expansion equation [Eq. (4)] and the equation for the dependence of the inflow velocity on latent heating and radiative cooling [Eq. (10a)]. The five underlying processes/terms in the schematic (Fig. 1) are the latent heating per unit area $Q_{\rm rad}/(\pi r_t^2)$, the radiative cooling per unit area $Q_{\rm rad}/(\pi r_t^2)$, u_t , turbulent friction $-C_d(\mu v_t)^2/h_w$, and $\partial v/\partial t$ at r_t . Our model prediction of each of these terms is shown in Fig. 6.

During the expansion stage, latent heating is significantly larger than radiative cooling. The latent heating rate can exceed 900 W m⁻² when the TC is small ($r_8 \approx 250$ km), which is also supported by the simulations in appendix C with $f = 5 \times 10^{-5}$ s⁻¹ (not shown). This amount of heating would induce ~ 8 K day⁻¹ temperature increase of the atmosphere (assuming constant pressure) without lateral energy/entropy exchange, whereas the actual average temperature change rate is on the order of 10^{-1} K day⁻¹ in a TC (estimated from the CTL simulation with $T_{\rm tpp} = 200$ K and $f = 5 \times 10^{-5}$ s⁻¹ in appendix C). Thus, the overturning circulation is needed to export excess latent

 $^{^{10}}$ This can be a $\sim\!20\%$ overestimate of q_{vb} as it does not account for the vertical profile of boundary layer q_v . This would lead to a $\sim\!200$ -km overestimate of $r_{t,\rm eq}$ in section 6c. Taking a vertical average from surface to 2 km of altitude (approximately the inflow depth associated with $M_{\rm ew}$) of the analytical saturation mixing ratio q_v^* profile of Romps [2016, his Eqs. (8) and (11)] appears to resolve this issue, though here we keep it simple and not adopting the Romps (2016) model.

 $^{^{11}}$ In simulations with $T_{\rm SST}=300$ K, $T_{\rm e,lat}$ and $T_{\rm e,rad}$ are about 275 K, though here we avoid specifying these values based on simulations for simplicity. Our approach yields $T_{\rm e,lat}\Delta s_d=T_{\rm e,rad}\Delta s_d=L_{\nu}q_{\nu b}$, i.e., a characteristic difference of the dry static energy between tropopause and the surface. This $\sim\!10\%$ overestimation $T_{\rm e,lat}$ and $T_{\rm e,rad}$ would induce a $\sim\!10\%$ overestimation of ξ and a $\sim\!55\text{-km}$ underestimate of $r_{\rm t,eq}$ in section 6c.

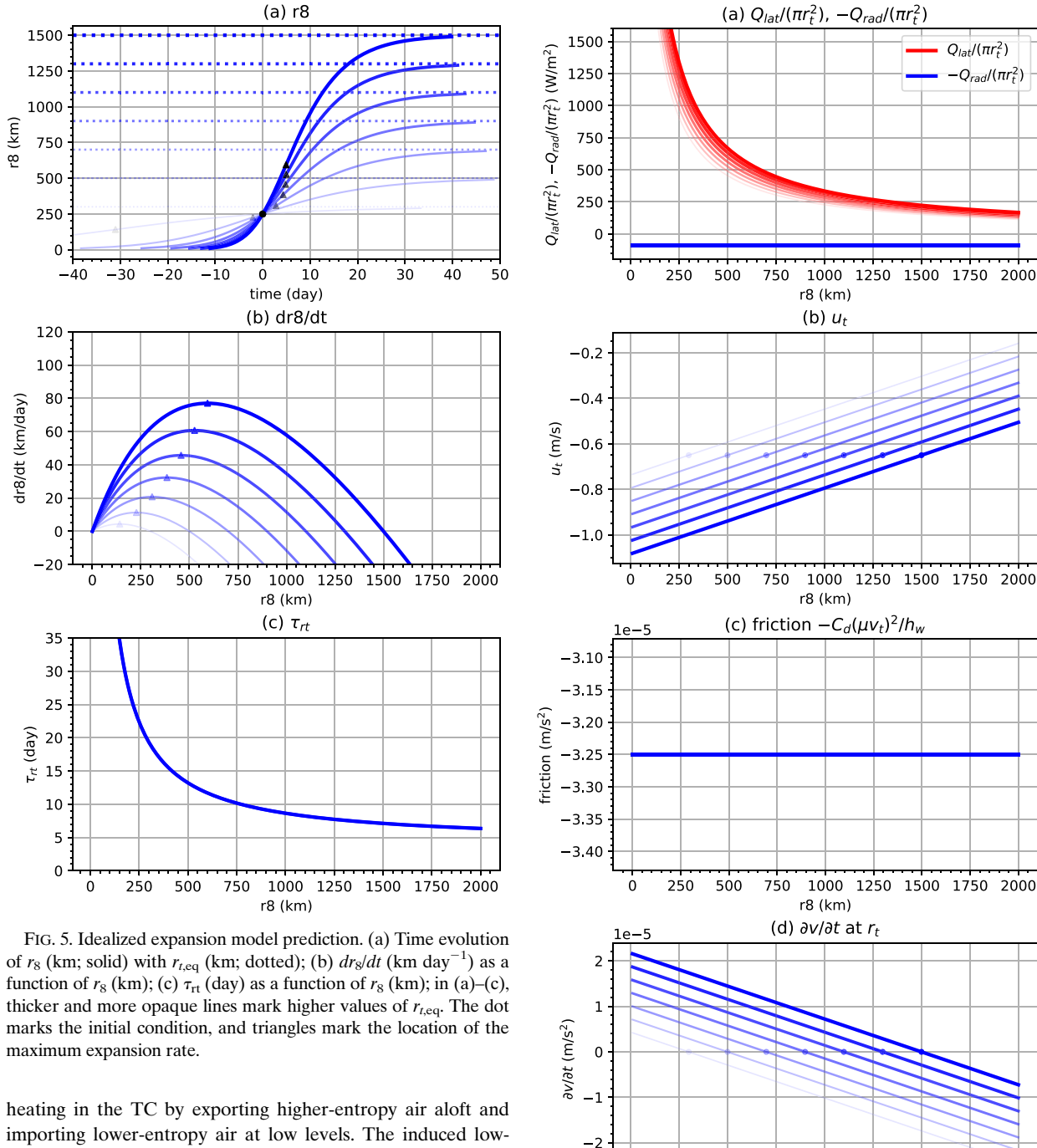


FIG. 6. As in Fig. 5, but for (a) latent heating per unit area $Q_{\text{lat}}/(\pi r_t^2)$ (W m⁻²; red) and radiative cooling per unit area $-Q_{\text{rad}}/(\pi r_t^2)$ (W m⁻²; blue), (b) radial velocity u_t (m s⁻¹), (c) $-C_d(\mu v_t)^2/h_w$ (m s⁻²), and (d) local spinup rate $\partial v/\partial t$ (m s⁻²) at r_t . The dots in (b) and (d) mark equilibrium.

importing lower-entropy air at low levels. The induced low-level inflow by this overturning circulation may be strong enough so that the local spinup at r_t is achieved and TC starts to expand. Quantity u_t linearly increases with r_t [Eq. (10)] with an equilibrium value of about -0.65 m s⁻¹ (Fig. 6b), which corresponds to zero local spinup. Friction at r_t is a constant by design at a value of $\sim -3.25 \times 10^{-5}$ m s⁻² (Fig. 6c). As a result, $\partial v/\partial t$ at r_t linearly decreases with size [Eq. (3)], such that an equilibrium is guaranteed.

It follows from Eq. (13) that larger $r_{t,\rm eq}$ corresponds to larger $Q_{\rm lat}$ (Fig. 6a), and thus, the quantity $Q_{\rm lat}/(\pi r_t^2) \sim 1/r_t$. Meanwhile, the quantity $Q_{\rm rad}/(\pi r_t^2)$ is a constant $\sim 89~{\rm W~m}^{-2}$.

Thus, there exists a TC size at which there is zero net heating in the TC, and thus the expansion rate must vanish before this radius is reached. At equilibrium itself, the area-integrated latent heating inside of $r_{t,eq}$ still slightly exceeds radiative cooling because the nonzero surface friction also exists [Eqs. (4) and (10)].

Finally, taking $\partial v/\partial t$ (Fig. 6d) and $\partial v/\partial r$ (Fig. 2) together, the expansion rate (Fig. 5c) peaks in the middle of expansion rather than the beginning because of the larger slope of the wind profile when the TC is small.

4. Comparison of theoretical prediction against simulations

a. Evaluating modeled expansion assuming known equilibrium size

In this subsection, we test our model's prediction for the time-dependent evolution of size against numerical simulations for the case where $r_{t,eq}$ is known. To do this, we set $r_{t,eq}$ constant and equal to the ensemble-mean equilibrium size of the simulated TC in each experiment to evaluate how well the analytical expansion model solution [Eq. (25)] can capture the first-order structure of expansion and its variations across experiments. We define $\tau_{\rm rt}$ using the parameters of the base environment in section 3a. Three sets of numerical simulations (see appendix C) are taken for comparison: one set varying the tropopause temperature $T_{\rm tpp}$ (TTPP), which modulates the potential intensity and V_{Carnot} , one varying f Coriolis parameter (FCOR), and one varying the ExSST, which also modulates the potential intensity and V_{Carnot} . CTL experiment is defined at $T_{\rm tpp} = 200 \text{ K}, T_{\rm SST} = 300 \text{ K}, \text{ and } f = 5 \times 10^{-5} \text{ s}^{-1}, \text{ correspond-}$ ing to TCs on real Earth. In simulations, r_8 is defined at 950 m of altitude.

1) COMPARISON WITH TTPP

The ensemble size evolutions across experiments for TTPP are shown in Fig. 7a (solid line and shading). The ensemblemean time series of r_8 (and other variables of interest) is calculated in the following manner in order to exclude the effect of possible different start times of expansion in different ensemble members. Time series of r_8 (and other variables of interest) in each ensemble member is shifted in time so that day 0 is the first day when r_8 exceeds an estimated value of halfequilibrium size, which is taken as half of the equilibrium (days 40–50) r_8 of ensemble index 0. Cases with $T_{\rm tpp}=174$, 187 K are neglected (here and throughout, except in section 6b) because their size evolution is very similar to $T_{\rm tpp} = 163$ K. It is seen that TC size increases with time for about 20 days and approaches an equilibrium, similar to the qualitative behavior of the ideal expansion model prediction in section 3a. We take the average of ensemble-mean r_8 during the last ten days of ensemblemean r_8 time series in TTPP as $r_{t,eq}$ for our expansion model; in this manner, the expansion model only needs τ_{rt} , which is the same as in section 3a (Fig. 5b) as determined by the same parameters as in section 3a.

To compare theory and simulation, we set r_{t0} and t_0 in our expansion model [Eq. (25)] to be the first ensemble-mean r_8

above $r_{t,eq}/2$ and the corresponding time in simulations, respectively, for all cases. This approach was used to compare intensification theory against simulations in Ramsay et al. (2020). The analytical model predictions of size evolution [Eq. (25)] are shown in dashed lines (Fig. 7a). The corresponding expansion rate in TTPP and that predicted by the expansion model is shown in Fig. 7b. Overall, there is a very good match between TTPP and the expansion model prediction. Higher $T_{\rm tpp}$ corresponds to smaller equilibrium r_8 and smaller peak expansion rate (Figs. 7a,b). The lone case that matches a bit less well is the 163 K case, which expands a bit more slowly than the theory predicts in the first half of expansion.

2) COMPARISON WITH FCOR

An equivalent comparison as in Fig. 7a is performed with FCOR (Fig. 7b). First, we note that equilibrium size in FCOR scales approximately with a 1/f scaling, with the time scale of expansion longer with lower f. Here, we define equilibrium size as the average ensemble-mean r_8 during the last 20 days for $f = 1.25 \times 10^{-5}$ and $f = 2.5 \times 10^{-5}$ s⁻¹, the last 10 days for $f = 5 \times 10^{-5} \text{ s}^{-1}$, the 20-day period ending 10 days before the end of the ensemble time coordinate for $f = 10 \times 10^{-5} \text{ s}^{-1}$, and the 5-day period ending 30 days before the end of the ensemble time coordinate for $f = 15 \times 10^{-5} \,\mathrm{s}^{-1}$. An earlier period is chosen for high f cases to capture their peak sizes. These equilibrium sizes are used as $r_{t,eq}$ for the expansion model. Analogous to our analysis for TTPP in Fig. 7a, the expansion model only needs τ_{rt} then, which is determined by the same parameters in section 3a. The lone exception is that τ_{rt} depends on f, which is set to the corresponding value in FCOR in each

The analytical solution of size evolution [Eq. (25)] is then compared with FCOR (Fig. 7c). Integration constants r_{t0} and t_0 are set in the same manner as Fig. 7a. The expansion rate in FCOR and that predicted by the expansion model is shown in Fig. 7d. Overall, the expansion model again compares reasonably well with the experiments in FCOR. The lone case that does not match as well is for $f = 1.25 \times 10^{-5} \, \mathrm{s}^{-1}$, which expands more gradually than predicted by the theory. Otherwise, the expansion model does reasonably well for $f = 2.5 \times 10^{-5} \, \mathrm{s}^{-1}$ (to a lesser extent for the early stage of expansion) and $f = 5 \times 10^{-5} \, \mathrm{s}^{-1}$ (and larger f), which are the principal latitudes (10° and 20°N) of TC development on Earth.

3) COMPARISON WITH EXSST

An equivalent comparison as in Figs. 7a and 7b is performed with ExSST (Figs. 7c,d). It is first noted that in ExSST when $T_{\rm SST}$ is higher, both the equilibrium size and expansion rates are higher (solid lines and shading of Fig. 7c). We define $r_{t,\rm eq}$ as the average ensemble-mean r_8 during the 10-day period ending 15 days before the end of the ensemble time coordinate for $T_{\rm SST}=286$ K, the last 10 days for $T_{\rm SST}=293$ and 300 K, and the 10-day period ending 10 days before the end of the ensemble time coordinate for $T_{\rm SST}=307$ K. Earlier periods are chosen for two cases to capture their peak sizes. Unlike comparison with TTPP and FCOR, to compare the expansion model prediction with ExSST, more parameters need

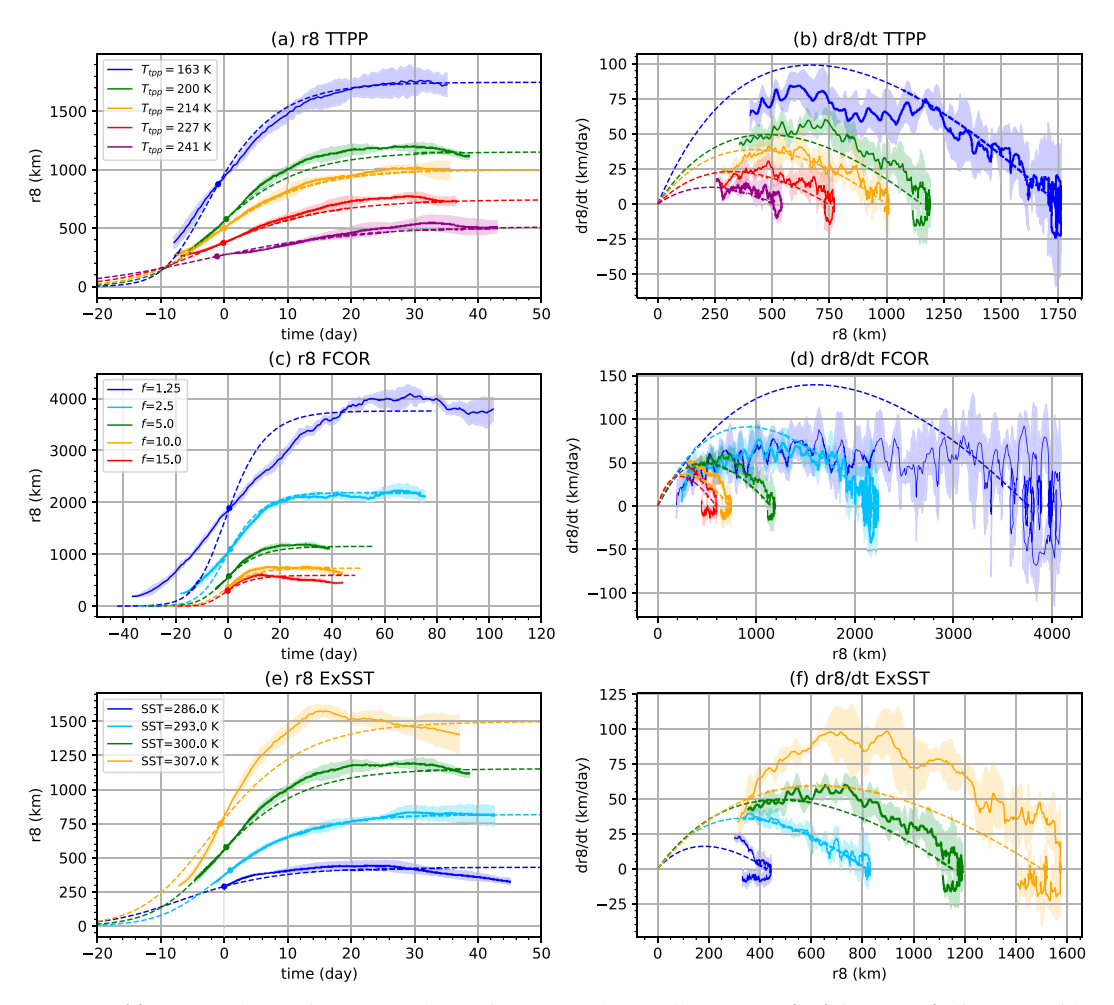


FIG. 7. (a) Temporal evolution of a 120-h running averaged ensemble-mean r_8 (km) in TTPP (solid; cases with $T_{\rm tpp} = 241, 227, 214, 200, 163$ K are shown) and analytical prediction of the expansion model (dashed) taking $r_{t,\rm eq}$ equal to equilibrium sizes of TTPP (see the text). The shading marks 1 standard deviation from ensemble mean. Dots mark the initial condition for the expansion model. (b) The corresponding expansion rate dr_8/dt (km day⁻¹) in TTPP (solid lines are ensemble mean of the 24-h expansion rate as a function of the 120-h running averaged ensemble-mean r_8 ; shading marks one standard deviation) and in the expansion model (dashed). (c),(d) As in (a) and (b), but for FCOR; (e),(f) As in (a) and (b), but for ExSST. Warmer color means higher values of the variable being varied (see the legend).

to be set according to different $T_{\rm SST}$. In particular, Δs_d , $T_{e,\rm rad}$, $T_{e,\rm lat}$, and ρ_i are set corresponding to $T_{\rm SST}$, ¹² so that we have the corresponding B in Eq. (25).

The expansion model predictions of r_8 evolution in comparison with ExSST are shown in dashed lines of Fig. 7e. The expansion model works nicely, except that the model struggles to fully capture the high expansion rate when $T_{\rm SST}=307$ K, though the expansion model does qualitatively correct predictions (Fig. 7f). We note that the peak ensemble-mean expansion rate r_8 in ExSST is ~25, 35, 55, 95 km day⁻¹ when $T_{\rm SST}=286, 293, 300, 307$ K, respectively.

Overall, the expansion model prediction compares fairly well with the simulation experiments in Fig. 7. We conclude the following:

- 1) Quantity $\tau_{\rm rt}$ provides a reasonable time scale for expansion (10–15 days for 20°N).
- 2) Quantity $r_{t,eq}$ can be assumed constant with respect to r_t (here r_8) given an environment defined by V_p (and V_{Carnot}) and f (to a lesser extent for 5° and 10° N).
- 3) The expansion model predicts a reasonable size evolution (and expansion rate) when T_{tpp} , T_{SST} , and f change.

b. Prediction of equilibrium size

The above subsection indicates that the expansion model works reasonably well given a known value of $r_{t,eq}$ taken from

¹² Quantity ρ_i is simply set proportional to T_{SST}^{-1} .

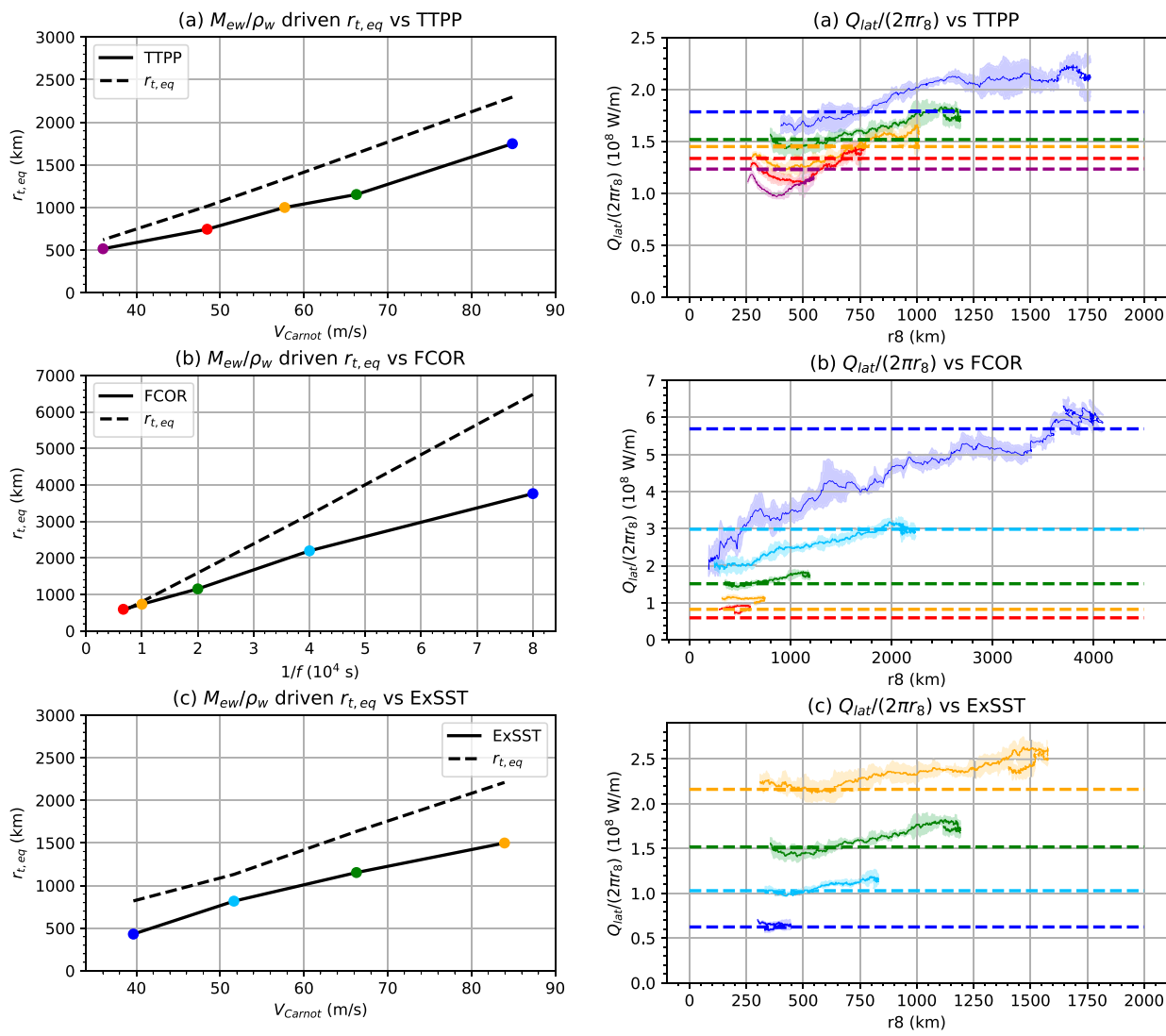


FIG. 8. (a) Ensemble-mean equilibrium sizes of TTPP simulations (solid) and the predicted $r_{t,eq}$ (dashed). (b) As in (a), but for FCOR. (c) As in (a), but for ExSST. Dots mark different cases in TTPP, FCOR, and ExSST. In (a)–(c), colors have the same meaning as Fig. 7.

the simulations. We next test how well the model can predict $r_{t,eq}$ from environmental parameters based on the parameterization of $(M_{ew}/\rho_w)_{eq}$ [Eq. (30)] in section 2d. The quantity V_{Carnot} in TTPP, FCOR, and ExSST is directly calculated with T_{SST} , T_{tpp} , and surface pressure (about 1012 hPa in CTL) from the initial state.

The resulting predictions for $r_{t,eq}$ are compared with the ensemble-mean equilibrium r_8 in TTPP (Fig. 8a), FCOR (Fig. 8b), and ExSST (Fig. 8c). The predictions for $r_{t,eq}$ reasonably follow the simulated values in TTPP, FCOR, and ExSST, with a closer match in TTPP and ExSST. Specifically, $r_{t,eq}$ increases with V_{Carnot} and is proportional to 1/f, though the latter dependence is a bit weaker than a pure linear dependence on 1/f. Thus, $r_{t,eq}$ can in principle be estimated from environmental parameters.

FIG. 9. (a) The term $\mathcal{Q}_{\text{lat}}/(2\pi r_8)(10^8 \text{ W m}^{-1})$ in TTPP (solid lines: ensemble mean; shaded: one standard deviation) and those correspondingly predicted by the expansion model (dashed; see the text for details). (b) As in (a), but for FCOR. (c) As in (a), but for ExSST. Colors have the same meaning as Fig. 7.

5. Evaluation of model foundation

a. Simplifying assumptions: constant $Q_{\rm lat}/(2\pi r_{\rm t})$ and constant $r_{\rm t,eq}$

The size-expansion model assumes constant $r_{t,eq}$, which comes from the assumption of constant $\mathcal{Q}_{lat}/(2\pi r_t)$ [see Eq. (13)]. In this subsection, we first assume whether $\mathcal{Q}_{lat}/(2\pi r_t)$ and $r_{t,eq}$ are approximately constant in simulations.

1) Constant $Q_{lat}/(2\pi r_t)$

The diagnosed $Q_{\rm lat}/(2\pi r_8)$ in TTPP, FCOR, and ExSST is shown in Fig. 9 (solid lines and shading). It is seen that $Q_{\rm lat}/(2\pi r_8)$ generally increases with expansion, but an

assumption of that being constant may not be considered unreasonable considering the relative variations of $\mathcal{Q}_{\mathrm{lat}}/(2\pi r_8)$ and r_8 itself. To evaluate how good the assumption of constant $\mathcal{Q}_{\mathrm{lat}}/(2\pi r_t)$ is, we seek $\mathcal{Q}_{\mathrm{lat}} \propto r_t^a$ at r_8 and see whether a is close to 1, compared to 2 (the $\mathcal{Q}_{\mathrm{rad}}$ scaling), with a obtained by linear regression. As a result, for TTPP, $a \approx 1.2$ for $T_{\mathrm{tpp}} = 163$, 200, 214, 227 K and $a \approx 1.1$ for $T_{\mathrm{tpp}} = 241$ K; for FCOR, $a \approx 1.4$, 1.2, 1.2, 1.0, 1.2 for $f = 1.25 \times 10^{-5}$, 2.5 $\times 10^{-5}$, 5×10^{-5} , 10×10^{-5} , 15×10^{-5} 1/s, respectively; for ExSST, a = 1.1, 1.2, 1.2, 1.1 for $T_{\mathrm{SST}} = 286$, 293, 300, 307 K, respectively. Values of a are all close to 1. Thus, the assumption of a constant $\mathcal{Q}_{\mathrm{lat}}/(2\pi r_t)$ is verified for r_8 in TTPP, FCOR (to a lesser extent for $f = 1.25 \times 10^{-5}$ s⁻¹), and ExSST.

In addition, also shown in Fig. 9 is the $Q_{\rm lat}/(2\pi r_8)$ predicted by Eq. (13b) given $r_{t,\rm eq}$ as in section 4a. It is seen that the expansion model [Eq. (13b)] reasonably reproduces both the qualitative dependence of $Q_{\rm lat}/(2\pi r_8)$ on $T_{\rm tpp}$, f, and $T_{\rm SST}$ and values of $Q_{\rm lat}/(2\pi r_8)$ themselves as well.

2) Constant $r_{t,eq}$

Though in the above analyses $r_{t,eq}$ has been treated as a time-independent constant, it can vary with time and size following Eq. (13b). The time-dependent $r_{t,eq}$ determined by Eq. (13b) using the ensemble mean of simulated $Q_{lat}/(2\pi r_8)$ and all other parameters same as in section 3a (except that f is set to the corresponding value in FCOR and the same treatment of parameters for ExSST as in section 4a) are examined; the results are shown in Fig. 10. It is seen that the time-dependent $r_{t,eq}$ generally increases with expansion, and the magnitude of the increase can be as large as $\sim 60\%$ in TTPP and ExSST. However, considering that the magnitude of size expansion of r_8 itself can be 300% of its initial value in TTPP and ExSST, then the assumption of $r_{t,eq}$ being constant may be considered reasonable in TTPP and ExSST.

In FCOR, this assumption holds reasonably for $f = 5 \times$ 10^{-5} s⁻¹ and larger values but does not hold for $f = 2.5 \times 10^{-5}$ 10^{-5} and $f = 1.25 \times 10^{-5}$ s⁻¹, in which the time-dependent $r_{t,eq}$ even approaches zero and negative values at the beginning of the expansion. This may explain why the expansion rate is overestimated by the expansion model in the early stage of the $f = 2.5 \times 10^{-5} \text{ s}^{-1}$ case and in the whole expansion period of the $f = 1.25 \times 10^{-5} \text{ s}^{-1}$ case (Fig. 7b). Notably, negative $r_{t,eq}$ is obviously incorrect. This simply indicates that, when f is small, the expansion model misses some important process (likely eddy momentum flux in the tangential wind budget) other than latent heating in favor of TC expansion while overestimating latent heating. Additionally, it is reasonable that Eq. (13b) does not produce the exact equilibrium sizes in simulations because of the simplifications of the expansion model.

b. Intermediate model predictions

In this subsection, the intermediate variables predicted by the expansion model underlying the final predictions in section 4a are given, along with their comparison with simulations. The intermediate variables are $\partial v/\partial r$, $\partial v/\partial t$, u_t at r_8 , and $\tau_{\rm rt}$.

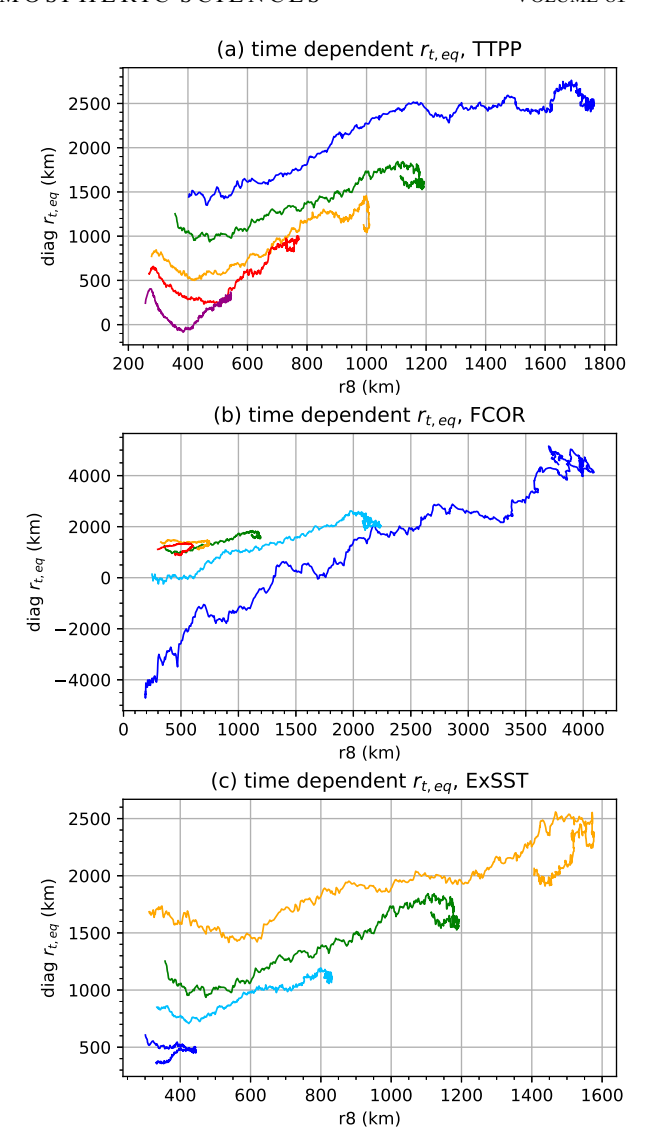
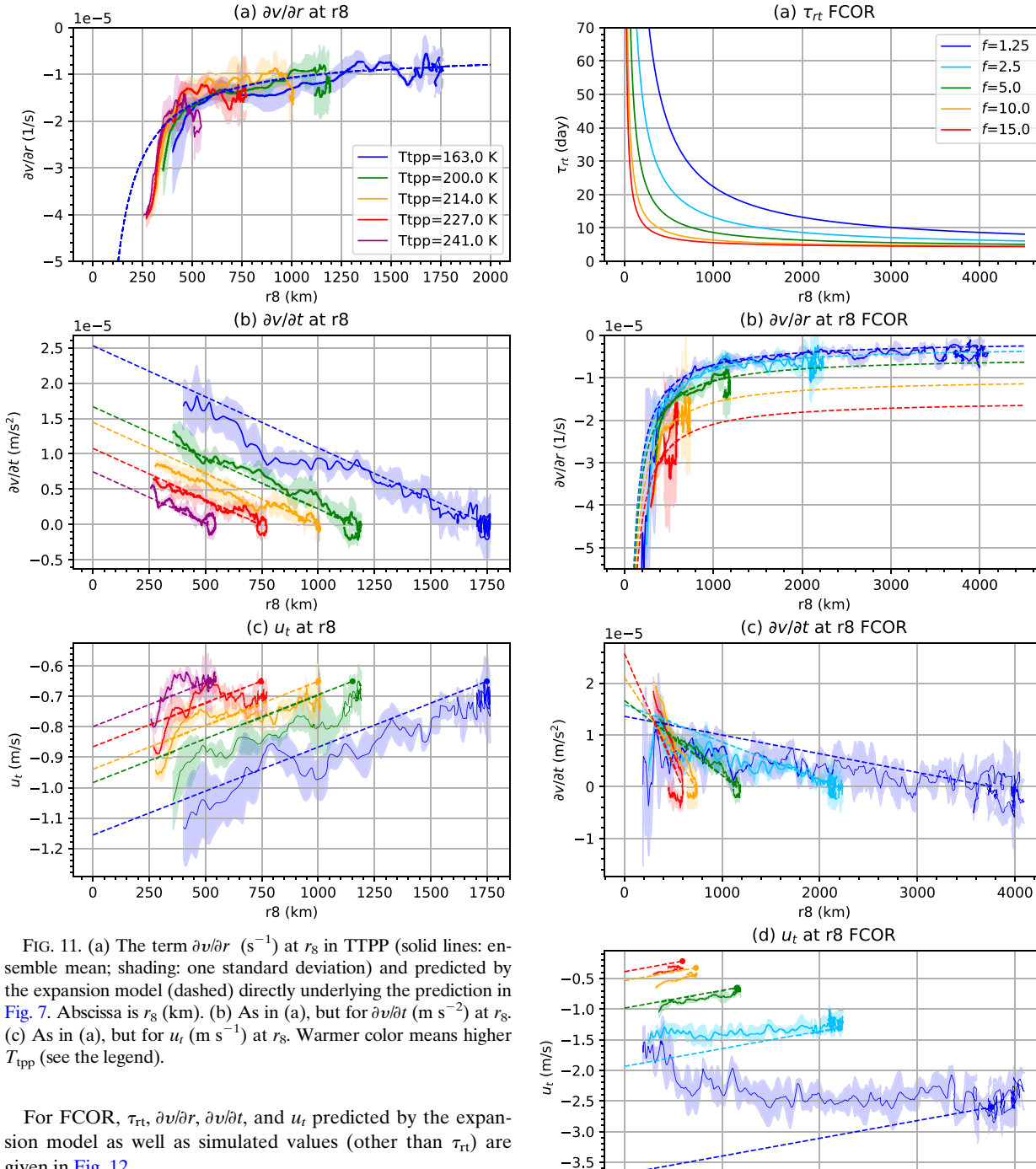


FIG. 10. Time-dependent $r_{t,eq}$ (km) as a function of r_8 (km) for (a) TTPP, (b) FCOR, and (c) ExSST. Colors in (a)–(c) have the same meaning as Fig. 7. See the text for details.

For TTPP, $\partial v/\partial r$, $\partial v/\partial t$, and u_t as well as those predicted by the expansion model are given in Fig. 11. It is seen that $\partial v/\partial r$ at r_8 predicted by the expansion model nicely matches TTPP, except that when $r_8 < 300$ km, $\partial v/\partial r$ decreases more rapidly in TTPP. There is no clear systematic dependence of $\partial v/\partial r$ on $T_{\rm tpp}$, consistent with the expansion model, in which $\partial v/\partial r$ is a single curve. The quantities $\partial v/\partial t$ and u_t at r_8 predicted by the expansion model also nicely match TTPP (Figs. 11b,c), which is systematically higher in magnitude with lower $T_{\rm tpp}$ and has similar slopes with respect to r_8 . This traces back to Eq. (10c), where $\partial u_t/\partial r_t = B/h_w$, which is a constant when $T_{\rm tpp}$ changes. Following Eq. (3), $(\partial/\partial r_t)(\partial v/\partial t|_{v=v_t}) = -f\partial u_t/\partial r_t$; thus, given f a constant (approximated absolute vorticity), then $(\partial/\partial r_t)(\partial v/\partial t|_{v=v_t})$ is a constant. Quantity $\tau_{\rm rt}$ for TTPP is the same as in Fig. 5.



given in Fig. 12. It is seen that $\tau_{\rm rt}$, which is proportional to 1/f and $-\partial \nu/\partial r$ at

 r_8 [Eq. (18)], increases as f decreases. Changing f also changes $\partial v/\partial r$ at r_8 (Fig. 12b). The wind profile is steeper (larger slope) for larger f, which is also observed in FCOR. Hence, the observation that $\tau_{\rm rt}$ increases monotonically as f decreases indicates that the effect of 1/f on $\tau_{\rm rt}$ dominates that of $(-\partial v/\partial r)$. Note that the difference of τ_{rt} will vanish for very large r_t as expected by the property of $[-(\partial v/\partial r)]$ in appendix B. The longer expansion time scale τ_{rt} with lower f in the expansion model is also consistent with the experiments in FCOR.

FIG. 12. (a) The τ_{rt} (day) for FCOR predicted by the expansion model directly underlying the prediction in Fig. 7. Abscissa is r_8 (km). (b)-(d) As in Figs. 11a-c, but for FCOR. Warmer color means higher f (see the legend).

2000

r8 (km)

1000

3000

4000

The expansion model also qualitatively correctly predicted the weaker dependence of $\partial v/\partial t$ at r_8 on r_8 when f is smaller (Fig. 12c) and the identical dependence of u_t at r_8 on r_8 when f varies (Fig. 12d). This also traces back to Eq. (10c). As B does not depend on f, thus $\partial u_t/\partial r_t$ is a constant; then, $(\partial/\partial r_t)(\partial v/\partial t|_{r=r_t})$ will be smaller when f is smaller [Eq. (3)]. A smaller magnitude of u_t in FCOR than predicted when $f=2.5\times 10^{-5}$ and $f=1.25\times 10^{-5}$ s⁻¹ is consistent with the weaker than predicted latent heating rate in these cases (Fig. 9).

The same analysis is repeated for ExSST (Fig. 13). First, it is seen that $\tau_{\rm rt}$ increases with $T_{\rm SST}$. From Eq. (18), $\tau_{\rm rt}$ is proportional to 1/B and $[-(\partial v/\partial r)]$ at $r_{\rm f}$. From Eq. (11b), it follows that 1/B closely follows the C–C scaling when $T_{\rm SST}$ varies. However, from Eq. (21), it is inferred that $[-(\partial v/\partial r)]$ should decrease, but with a speed more slowly than the inverse C–C scaling, with $T_{\rm SST}$, because 1/B appears in both numerator and denominator. This explains that $\tau_{\rm rt}$ increased with increased $T_{\rm SST}$. Correspondingly, the expansion model correctly predicts the decrease of the magnitude of $\partial v/\partial r$ at r_8 when $T_{\rm SST}$ increases (Fig. 13b). The prediction is also quantitatively reasonable.

For $\partial v/\partial t$ at r_8 in ExSST (Fig. 13c), it is seen to start from similar values when r_8 is small but decreases more slowly with r_8 when $T_{\rm SST}$ is larger, which is seen qualitatively predicted by the expansion model. This is in contrast with TTPP, where $(\partial/\partial r_t)(\partial v/\partial t)$ is approximately the same (Fig. 11). Qualitatively speaking, $Q_{\rm lat}/(2\pi r_8)$ and Δs_d both (roughly for the former) follow the C-C scaling, and then, the first term of the RHS of Eq. (10) should not change much with T_{SST} . This indicates that when r_t is small, u_t and thus $\partial v/\partial t$ should be approximately the same when T_{SST} varies. Similar to the analysis for TTPP and FCOR, $\partial u_t/\partial r_t = B/h_w$ and B decreases with T_{SST} following the inverse C-C scaling; thus, assuming absolute vorticity roughly the same (compared to the C–C scaling), then $\partial v/\partial t$ at r_8 decreases more slowly with r_8 when T_{SST} is larger. For u_t , it is first noted that the predicted u_t starting from similar values and decreasing more slowly with r_8 with increasing T_{SST} is supported by ExSST to some extent. However, it is noticed that the equilibrium values of u_t increase with T_{SST} , whereas they are identical as predicted by the expansion model. This may be explained by the relative vorticity at r_8 , which increases with $T_{\rm SST}$ (it can be inferred from Fig. 13b), with the same f. Thus, from Eq. (2), the equilibrium u_t should increase with T_{SST} . Such behavior is not captured by the expansion model because the relative vorticity is neglected (assumed much smaller than f) in Eq. (3).

Finally, comparing $\partial \upsilon/\partial t$ and $\partial \upsilon/\partial r$ at r_8 , it is concluded that the dependence of $\partial \upsilon/\partial r$ on $T_{\rm SST}$ contributes considerably to the faster peak expansion rate with higher $T_{\rm SST}$ in ExSST (Fig. 7).

6. Further physical interpretation of the model

a. Physical meaning of $r_{t,eq}$

Equation (13a) provides an expression for equilibrium size, which is derived independently of TC PS (Wang et al. 2022)

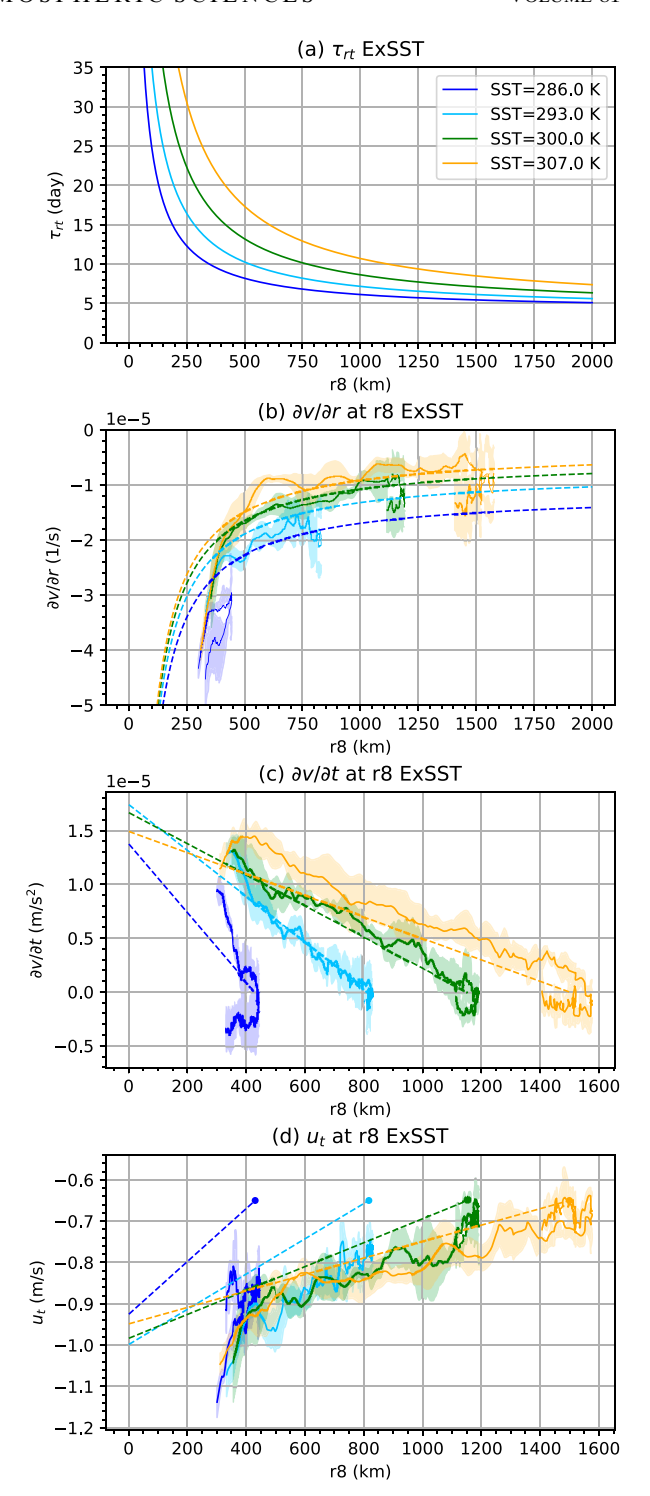


FIG. 13. (a) The $\tau_{\rm rt}$ (day) for ExSST predicted by the expansion model directly underlying the prediction in Fig. 7. Abscissa is r_8 (km). (b)–(d) As in Figs. 11a–c, but for ExSST. Warmer color means higher $T_{\rm SST}$ (see the legend).

but shares many similar properties. In this subsection, we further quantitatively discuss the physical meaning of $r_{t,eq}$.

In essence, $r_{t,eq}$ principally depends on (or is reflected by) latent heating rate, radiative cooling rate, Δs_{d} , and f [Eq. (13b)]. All else being equal, $r_{t,eq}$ scales directly with $\mathcal{Q}_{\text{lat}}/(2\pi r_{t})$ [Eq. (13b)], and hence, a larger equilibrium size should be associated with a larger $\mathcal{Q}_{\text{lat}}/(2\pi r_{t})$ throughout the expansion. This is evident in the TTPP experiments: $\mathcal{Q}_{\text{lat}}/(2\pi r_{8})$ is indeed systematically higher with lower T_{tpp} , corresponding to larger equilibrium sizes (Fig. 9a, solid lines), which is also correctly predicted by the expansion model, demonstrating that the larger latent heating rate during the expansion leads to larger equilibrium size. For TTPP, the enhanced latent heating rate arises principally because of the enhanced overturning mass flux [Eq. (8)], which is larger at higher potential intensity [Eq. (30)]. And this also leads to a higher expansion rate of TCs with lower T_{tpp} , consistent with the analysis in section 3a.

Similar dependencies are evident when f is varied. Since $r_{t,\text{eq}}$ scales as 1/f [Eqs. (15), (16), and (30)], $Q_{\text{lat}}/(2\pi r_t)$ should also scale with 1/f [Eq. (13b)]. This is found to be qualitatively true in both FCOR (Fig. 9b, solid lines) and the expansion model prediction (Fig. 9b, dashed lines). The $f = 1.25 \times 10^{-5} \, \text{s}^{-1}$ simulation case deviates more strongly in that this quantity is substantially smaller than the model predicted value during the main expansion stage when $f = 1.25 \times 10^{-5} \, \text{s}^{-1}$; this is consistent with its deviation from the model prediction of size itself discussed in section 3a.

When $T_{\rm SST}$ increases, Δs_d increases. As a result, $\mathcal{Q}_{\rm lat}$ needs to increase (roughly following the C–C scaling) to achieve an increase of $r_{t,\rm eq}$ in ExSST (Fig. 9c). As Δs_d also varies with $T_{\rm SST}$, $r_{t,\rm eq}$ cannot be inferred from $\mathcal{Q}_{\rm lat}$ alone when $T_{\rm SST}$ is changing.

To summarize, in the expansion model, equilibrium size is effectively modulated by $\mathcal{Q}_{\mathrm{lat}}/(2\pi r_t)$, and the expansion rate is modulated by the equilibrium size. For a given initial size and environment, a larger $\mathcal{Q}_{\mathrm{lat}}/(2\pi r_t)$ translates to a larger $r_{t,\mathrm{eq}}$ and thus a larger expansion rate. In practice, if a TC moves to a more favorable environment for convection, then its expansion rate would be expected to increase and its expected equilibrium size also increases, as quantitatively described by Eq. (13b). This interpretation is consistent with the behavior of observed storms, which have been found to expand when convection is enhanced outside of the storm inner core across a variety of distinct forcing mechanisms (Maclay et al. 2008).

The dependence of $r_{t,eq}$ on the latent heating rate $[\mathcal{Q}_{lat}/(2\pi r_t)]$ is complementary to the TC PS model, with the former being a reflection of the volume (or mass)-integrated processes of the system instead of a single parcel's cycle. As noted above, the larger latent heating rate produces a larger $r_{t,eq}$ (with the same f and T_{SST}) as it is associated with a larger V_p , consistent with V_{Carnot}/f scaling (Wang et al. 2022). Meanwhile, the

effect of C_d in the size scaling is rather small because an increase of C_d reduces the storm intensity but increases the inflow angle and the inflow depth under the eyewall at the same time, such that $M_{\rm ew}$ remains relatively constant.

b. Expansion mechanism

The model [Eq. (12)] physically assumes that TC size expansion is driven principally by latent heating, which drives the low-level lateral inflow that imports absolute vorticity to expand the storm. In this section, we test how the model predicts the dependencies of the inflow velocity u_t , the local spinup rate $\partial v/\partial t$, and the expansion rate dr/dt on the latent heating rate in a given $T_{\rm SST}$ and how they are compared with simulations. In this subsection, TTPP will be used as a demonstration as TTPP provides the cleanest test; FCOR will be supplementary; ExSST does not serve as a material for the test because $\mathcal{Q}_{\rm lat}$ and Δs_d , which have compensating effects, are both changing.

While the final version of the model is predictive based on the environmental parameters alone, the model also provides a quantitative dependence of a response of expansion rate to a change of latent heating \mathcal{Q}_{lat} in a given environment. Equations (1), (3), and (10) indicate that all else being equal, an increase of latent heating leads to an increase in the lateral inflow magnitude and thus the expansion rate. This understanding is useful when a TC experiences an inner-core structural variation such as the secondary eyewall formation (e.g., Kossin and Sitkowski 2009), which may lead to a size expansion.

Manipulating Eq. (10) gives that for a given r_t , $\partial u_t/\partial (\mathcal{Q}_{lat}/\pi r_t^2) \propto r_t$. It follows that $[\partial/\partial (\mathcal{Q}_{lat}/\pi r_t^2)](\partial v/\partial t) \propto fr_t$ and $\left[\partial/\partial(\mathcal{Q}_{|at}/\pi r_t^2)\right](dr_t/dt) \propto \left[-(\partial v/\partial r)\right]^{-1} fr_t$ at that given r_t . The linear relations are compared with TTPP, shown in Fig. 14. The r_8 is first taken as 550 km, and data in TTPP are collected with r_8 from 500 to 600 km (Figs. 14a-c). This size corresponds to the relatively large (above median ~400 km; Schenkel et al. 2023) TCs on Earth. We see an overall nice match of both the slope (sensitivity) and the absolute value between the expansion model prediction (baseline environment setting) and TTPP for all of u_t , $\partial v/\partial t$, and dr_8/dt . TCs with lower T_{tpp} in TTPP are associated with larger latent heating rate, which leads to stronger inflow velocity, local spinup rate, and expansion rate, consistent with the evolution of r_8 in Fig. 7. This also supports the overall hypothesis of the expansion model that latent heating drives expansion. Note that the expansion rate is rather sensitive to latent heating. For $Q_{lat}/(\pi r_8^2) = 500 \text{ W m}^{-2} \text{ in Fig. 14c } (dr_8/dt \approx 40 \text{ km day}^{-1};$ see the dotted fitting line), a 20% change of latent heating may either double the expansion rate $[dr_8/dt \approx 75 \text{ km day}^{-1}]$ with $Q_{lat}/(\pi r_8^2) = 600 \text{ W m}^{-2}$] or terminate expansion [with $Q_{\text{lat}}/(\pi r_8^2) = 400 \text{ W m}^{-2}$].

The same analysis is repeated but with $r_8 = 350$ km in the expansion model and r_8 from 300 to 400 km in TTPP (Figs. 14d–f). This size corresponds to relatively small (below median) TCs on Earth. The predictions of u_t and $\partial v/\partial t$ as linear functions of $Q_{\text{lat}}/(\pi r_8^2)$ are still generally valid, except that the discrepancy for dr_8/dt appears larger compared to $r_8 = 550$ km (Figs. 14a–c).

¹³ Quantity Q_{lat}/r_t is completely determined by $r_{t,eq}$ through Eq. (13b). Thus, the present model does not allow Q_{lat} to deviate from its "expected" value, though it can happen in nature

its "expected" value, though it can happen in nature.

14 When $T_{\rm SST}$ changes, Eq. (13b) can only predict the minimum increase of $Q_{\rm lat}$ to maintain the same $r_{t,\rm eq}$. In this sense, the TC PS model is more powerful.

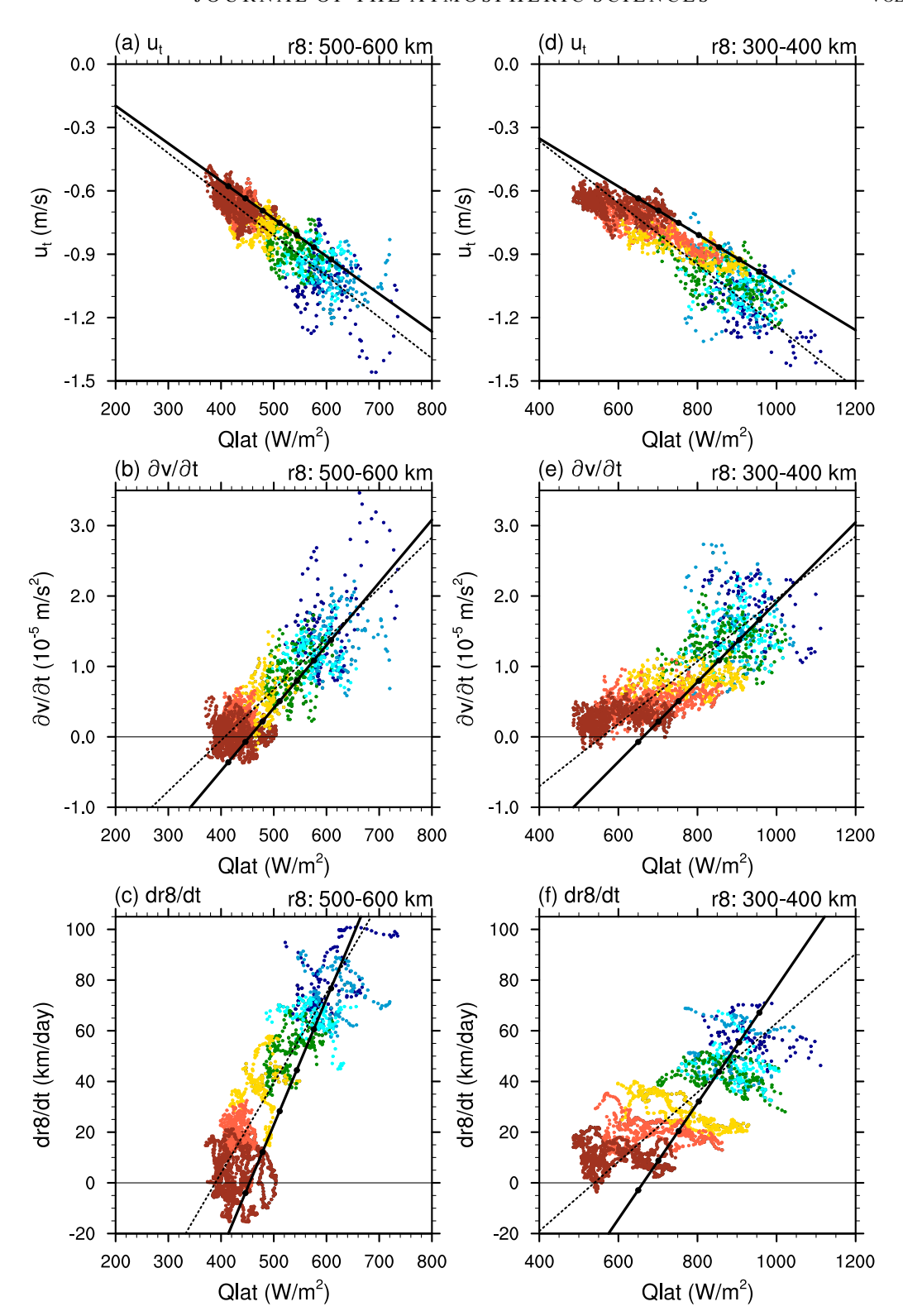


FIG. 14. (a) Colored dots show u_t (m s⁻¹) and $Q_{\rm lat}/(\pi r_8^2)$ (W m⁻²) when r_8 is above 500 km and below 600 km in TTPP (all ensemble members); warmer color means higher $T_{\rm tpp}$. The black line shows the expansion model prediction (baseline environment setting) with $r_8 = 550$ km, and black dots mark cases in Figs. 5 and 6. The dotted line is a linear regression fitting to the centroids of each cluster (each $T_{\rm tpp}$ value). (b) As in (a), but for $\partial v/\partial t$ (m s⁻²) at r_8 . (c) As in (a), but for dr_8/dt (km day⁻¹), shown as the 24-h expansion rate of the 120-h running averaged r_8 . (d)–(f) As in (a)–(c), but with $r_8 = 350$ km in the expansion model and r_8 from 300 to 400 km in TTPP. Note all cases in TTPP are shown.

This discrepancy likely arises from a bias in representing the tangential wind budget.

The dependence of u_t on the latent heating rate can also be tested against FCOR, as (also at constant r_t) $\partial u_t/\partial [\mathcal{Q}_{\text{lat}}/(\pi r_t^2)]$ does not depend on f {but $\partial (\partial v/\partial t)/\partial [\mathcal{Q}_{\text{lat}}/(\pi r_t^2)]$ and $\partial (dr_8/dt)/\partial [\mathcal{Q}_{\text{lat}}/(\pi r_t^2)]$ depend on f}. Analogous to the comparison for TTPP in Fig. 14, the comparison is shown in Fig. 15. The expansion model matches the simulations in both the absolute value and the slope of the relations reasonably well. Notably, the latent heating rate is substantially larger with smaller f, consistent with Fig. 9b.

Physically, the correspondence of high \mathcal{Q}_{lat} to low T_{tpp} and low f may be explained by the corresponding high frictionally induced eyewall updraft mass flux. For low T_{tpp} , it is the high intensity that is likely most responsible (Xi et al. 2023); for low f, it is the low boundary layer inertial stability that is likely most responsible (Smith et al. 2015; Li et al. 2023).

Overall, then, the expansion model can predict the dependence of u_t , $\partial v/\partial t$, and dr_8/dt on the latent heating rate, especially for u_t . This provides experimental evidence that the lateral inflow velocity and its resulting spinup are indeed driven principally by latent heating in the TC, with their quantitative dependence described by Eq. (10).

c. Model parameters

1) SENSITIVITY TO Δs_d

In this subsection, we test the sensitivity of the expansion model (section 2) to Δs_d , an important parameter that modulates both $r_{t,eq}$ [Eq. (16)] and τ_{rt} [Eq. (18)] through B. Increasing Δs_d decreases B, which decreases $r_{t,eq}$ and increases τ_{rt} , which both cause the expansion rate to decrease [Eq. (12)].

Physically, the overturning acts to export entropy because the inflow brings in lower entropy air while the outflow takes out higher entropy air. This depends on Δs_d . If Δs_d is larger, then the overturning circulation can be less intense to achieve the same net export, which means smaller magnitude of the inflow velocity and hence slower expansion. The expansion model works reasonably partly because in a mature TC, the main portion of the inflow mass flux is confined to low levels. Hence, overturning circulations are very efficient at exporting entropy; this behavior can be characterized as having a strongly positive (i.e., stable) gross moist stability (Raymond et al. 2009).

To perform the sensitivity test, we vary Δs_d about the base value (187.1 J K⁻¹ kg⁻¹) in section 3 by multiplying it by 0.5, 0.75, 1.0, 1.25, and 1.5. In the calculation, $\partial v/\partial r$ is not modified (and hence ξ_0 remains fixed to the value in section 3, though A, B, and ξ vary with Δs_d) for simplicity. The quantity $r_{t,eq}$ is determined by the $(M_{ew}/\rho_w)_{eq}$ [Eq. (30)] in the base environment through Eqs. (15) and (16).

The results are shown in Fig. 16. When Δs_d varies from 50% to 150% of its base value, $r_{t,eq}$ decreases from 2000 to 1300 km; the quantity τ_{rt} increases by a factor of 3. The expansion rate decreases from about 250 km day⁻¹ to below 50 km day⁻¹. Though the overall values of the expansion rate $r_{t,eq}$ and τ_{rt} are still reasonable, it is evident that the expansion process

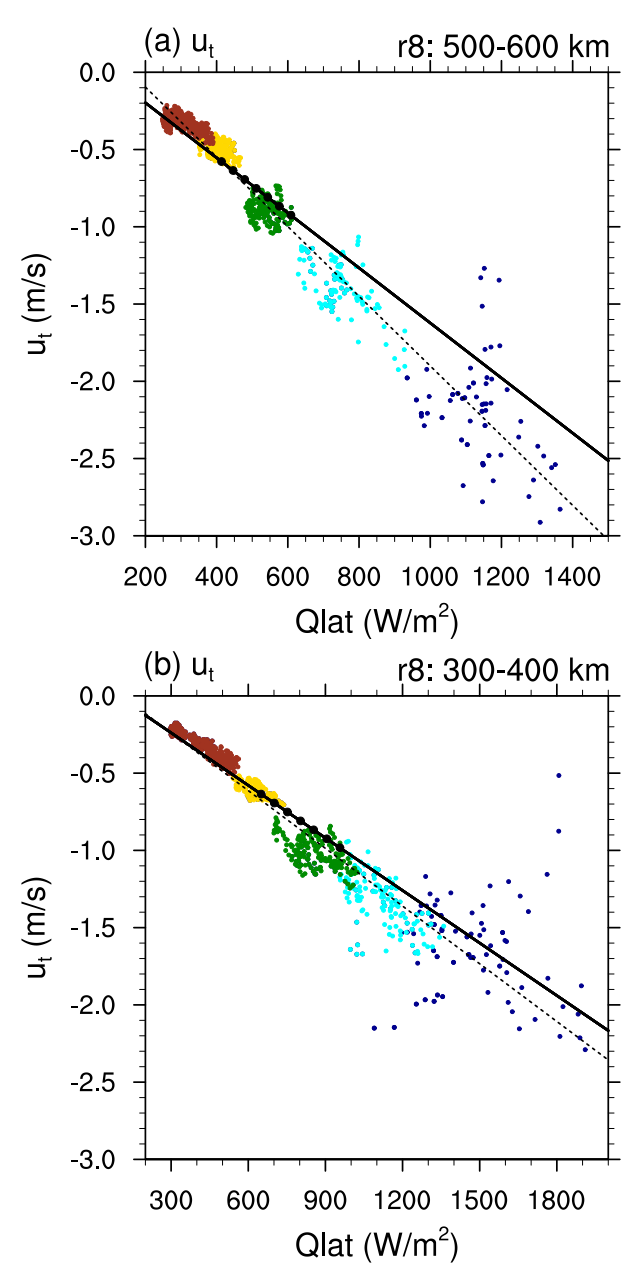


FIG. 15. (a) Colored dots show u_t (m s⁻¹) and $Q_{\rm lat}/(m_8^2)$ (W m⁻²) when r_8 is above 500 km and below 600 km in FCOR (all ensemble members); warmer color means higher f. The black line shows the expansion model prediction with $r_8 = 550$ km, and black dots mark cases in Figs. 5 and 6. The dotted line is a linear regression fitting to the centroids of each cluster (each f value). (b) As in (a), but with r_8 above 300 km and below 400 km for FCOR and $r_8 = 350$ km for the expansion model.

can be directly modulated by Δs_d . This implies that in a warmer climate, a likely increase of Δs_d would partially offset the effect of an increase of the latent heating rate that drives faster expansion (this is already reflected by an increase of $\tau_{\rm rt}$ with higher $T_{\rm SST}$ in Fig. 13). More realistic simulations of TC

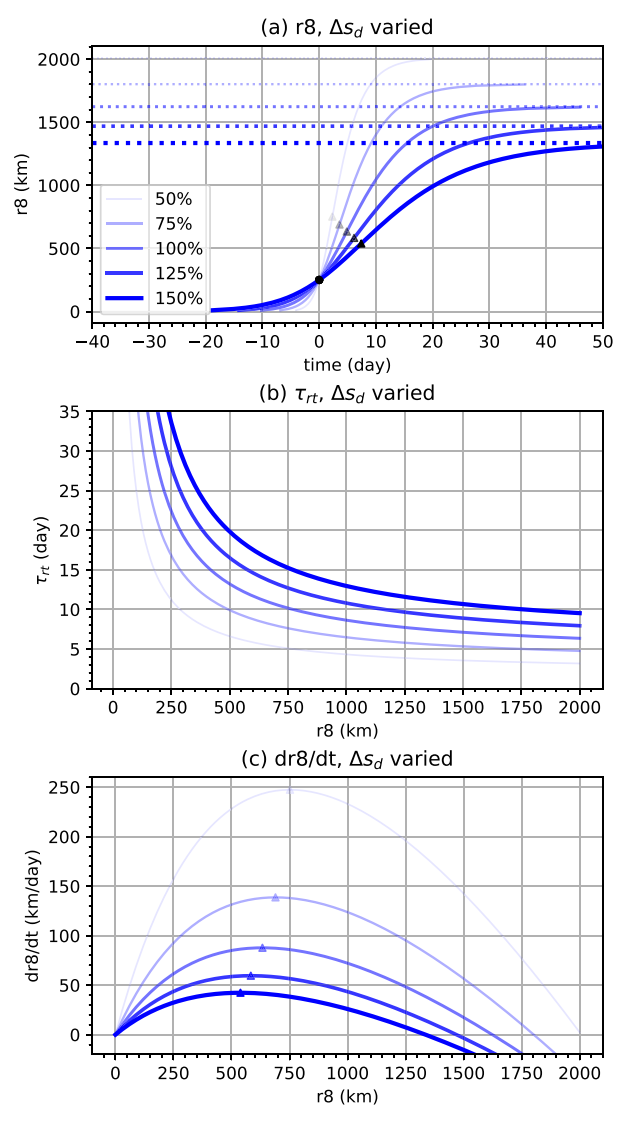


FIG. 16. As in Fig. 5, but with Δs_d varied from 50% to 150% of its base value with an interval of 25%; see the text for details. In (a)–(c), thicker and more opaque lines mark higher values of Δs_d .

evolution in a warmer climate are an important avenue of future work.

2) SENSITIVITY TO OTHER PARAMETERS

In this subsection, we provide a discussion of model sensitivity to other parameters. The expansion rate is proportional to $(r_{t,eq}-r_t)$ and $1/\tau_{rt}$ [Eq. (12)]. The quantity τ_{rt} is proportional to $[-(\partial \upsilon/\partial r)]$ at r_t , h_w , 1/f, and 1/B. The magnitude of $[-(\partial \upsilon/\partial r)]$ decreases with ξ_0 (= ξ) (see appendix B), with a specific example given in Fig. 2. The quantity $h_w = 2.5$ km is considered a fixed value and should not vary because it is tightly linked to the value of Δs_d (see appendix D). Parameter B is inversely proportional to Δs_d , which follows the C–C scaling.

If $r_{t,eq}$ needs to be predicted solely from environmental parameters, then Eq. (16b) indicates that $r_{t,eq}$ increases with $r_{RCE,eq}$ and

decreases with ξ . The quantity $r_{\text{RCE,eq}}$ depends on A/B and $(M_{\text{ew}}/\rho_w)_{\text{eq}}$, and Eq. (15) yields that $\partial \ln r_{\text{RCE,eq}}/\partial \ln A = 1/2$ and $\partial \ln r_{\text{RCE,eq}}/\partial \ln B = -1/2$; the quantity $(M_{\text{ew}}/\rho_w)_{\text{eq}}$ is proportional to V_{Carnot}^2/f^2 [Eq. (28)]. Figure 16 shows how $r_{t,\text{eq}}$ depends on ξ . Figure 8 provides examples of how environmentally predicted $r_{t,\text{eq}}$ depends on T_{tpp} , T_{SST} , and f.

7. Summary and discussion

In this paper, a predictive analytic model for the tropical cyclone size expansion on the f plane is proposed and its overall behavior is tested against numerical simulations varying tropopause temperature (TTPP), Coriolis parameter (FCOR), and sea surface temperature $T_{\rm SST}$ (ExSST). The expansion rate is described by a simple kinematic relation and is equal to the ratio of the local spinup rate of the tangential wind $(\partial v/\partial t)$ at outer radius r_t to the negative slope of the wind profile at that radius. The model predicts that size expansion is driven by latent heating (dominated by the eyewall) and suppressed by radiative cooling. This prediction is achieved by combining the tangential velocity budget at r_t with the volume-integrated entropy (heat) budget inside of r_t , with the two linked via a simple relationship between outer storm size and the upward mass flux of the overturning circulation. Area-integrated latent heating is proportional to r_t , while area-integrated radiative cooling is proportional to r_t^2 , such that the storm size eventually reaches an equilibrium $(r_{t,eq})$. The size-expansion rate is the ratio of the difference between $r_{t,eq}$ and the present size to a time scale τ_{rt} , and both parameters may be defined from environmental parameters alone. Key takeaways are as follows:

- The model yields a predictive, analytic solution for the evolution of storm size toward its equilibrium size (both larger or smaller than the present size) given the environmental parameters and an external set $r_{t,eq}$. This solution performs well in predicting the simulated size evolutions and expansion rates in simulations across a range of values of tropopause temperature, sea surface temperature (and hence potential intensity), and Coriolis parameter.
- The model successfully produces a characteristic expansion rate for r₈ of tens of kilometers per day with reasonable environmental parameters (Fig. 5), in line with past work using data for historical storms.
- The model predicts that the local spinup rate decreases quasi-linearly with expansion and that $\partial v/\partial r$ at r_8 decreases in magnitude with expansion, both consistent with simulations. The results taken together explain why the expansion rate peaks during the early-to-mid stages of expansion rather than at the beginning, as seen in simulations.
- The model predicts the reasonable time scale $\tau_{\rm rt}$ of 10–15 days when $f = 5 \times 10^{-5} {\rm s}^{-1}$, $T_{\rm SST} = 300 {\rm K}$, and the radiative cooling rate 1 K day⁻¹. The time scale is constant when varying $T_{\rm tpp}$ and larger when f is smaller, consistent with simulations.
- The model predicts that the equilibrium size r_{t,eq} increases with \(\sqrt{w}_{\cool} C_d^{-0.07} V_{\text{Carnot}} / f \), which is a scaling for the square root of equilibrium eyewall updraft mass flux and r_{0.eq}. The

quantity $r_{t,eq}$ is directly linked to the latent heating rate within the TC volume and is complementary to the TC potential size of Wang et al. (2022) while providing clearer mechanistic insight into the process of expansion.

- The model predicts that enhanced latent heating will cause the storm to expand faster (in a given environment), consistent with past observational work, finding that storms tend to expand significantly after convection is forced outside of the eyewall regardless of the forcing mechanisms (Maclay et al. 2008).
- The model provides a mechanistic understanding of why TC size expands toward an equilibrium in the first place: The overturning circulation exports excess latent heating in the TC when it is sufficiently small, and the resulting induced low-level inflow that imports absolute vorticity into the volume in excess to surface friction spins up the tangential wind in the outer circulation. As a result, the TC expands.

Here, we have taken a number of parameters as constant across our tests for simplicity to arrive at an analytically tractable model that appears to capture the first-order behavior of the dynamics of TC size. In reality, such parameters may not be perfectly constant (both in time and across experiments), a topic that could be more carefully examined within the simulations presented in this paper. Here, we have evaluated this assumption for a few key parameters, but additional detailed tests of the model assumptions as well as quantifying model parameters in simulations could be tackled in a future study.

This model offers a valuable foundation for better understanding and predicting changes in storm size on Earth. For example, it is known that TCs will shrink in the absence of convection with nonzero β (meridional gradient of f) due to radiation of planetary Rossby waves (Chavas and Reed 2019; Lu and Chavas 2022). How this shrinking effect alters the evolution of TC size on the f plane is an important question for predicting changes in TC size in nature. Incorporation of the β effect in the expansion model is a valuable avenue for future work.

One key assumption of the present model is the existence of an equilibrium TC outer size $r_{t,eq}$ that depends on environmental parameters on the f plane. Though a short-term equilibrium of size does exist in our simulations, a long-term existence/maintenance of equilibrium size is not conclusive in literature: Persing et al. (2019) pointed out that long-term (longer than tens of days) maintenance in limited domains may require an artificial source of relative angular momentum. However, in the present expansion model, $r_{t,eq}$ is valid and well defined at any particular instance and does not require that this radius remains constant for all time (it is able to maintain for about 10 days or potentially longer in our simulations). Nonetheless, an understanding of $r_{t,eq}$ in the context of long-term TC maintenance in limited domains remains an open question.

One open mechanistic question that we did not analyze in detail is the connection between potential intensity and updraft mass flux. In our simulations, the expansion rate increases with V_p (by lowering $T_{\rm tpp}$) consistent with our theory, and the majority of the condensational heating within r_8 does occur within the eyewall (appendix D). Hence, it is likely that V_p modulates the strength of overturning circulation in the eyewall by modulating TC intensity, which in turn modulates boundary layer frictional convergence. However, we do not explicitly quantify the eyewall dynamics in the present model. This also simplifies the problem a bit because potential intensity theory exists to describe the eyewall structure and successfully predicts a characteristic maximum wind speed, whereas the rainband activity is much less well understood and is much harder to predict. Correspondingly, although the rainband activity has been reported to effectively modulate TC size expansion, it is not actively predicted in the present model and is only parameterized by a constant α_p .

Finally, we note that the proposed expansion model predicts that the expansion rate is a function of present size [Eq. (23)], and hence, it is independent of the preceding history of storm size including initial vortex size. This is supported by an additional set of experiments varying initial vortex size and intensity (see the online supplemental material), suggesting that V_p ($V_{\rm Carnot}$) may be a more effective factor than the initial vortex structure to modulate the size-expansion rate.

Acknowledgments. We thank four anonymous reviewers for their constructive comments that help greatly enhance the manuscript. This work is supported by the National Science Foundation (NSF) AGS Grant 1945113.

Data availability statement. Description of the CM1 model is available at https://www2.mmm.ucar.edu/people/bryan/cm1/. The specific CM1v19.2 model code with the noted modifications and the namelist for CTL simulation used in this study have been uploaded to figshare with https://doi/org/10.6084/m9.figshare.22674361.

APPENDIX A

E04 Model and Its Relation to Expansion Model

The E04 model provides the near-surface wind profile through a slab boundary layer model in the subsidence region where the net vertical velocity is typically negative and is expressed as

$$\frac{\partial v}{\partial r} = \frac{2C_d r v^2}{w_{\text{cool}}(r_0^2 - r^2)} - f - \frac{v}{r},\tag{A1}$$

where $w_{\rm cool}$ is a constant clear-air subsidence velocity (positive downward) induced by radiative cooling. In the model, $\partial v/\partial r$ is determined locally by the inflow mass flux and

¹⁵ Thus, we do expect V_p to represent a characteristic intensity of the TC (see the supplemental material), though the exact relation between V_p and maximum wind speed is not considered here (see the discussion of superintensity in Persing and Montgomery 2003; Li et al. 2020).

friction and the inflow mass flux is determined by the accumulated subsidence mass flux outward.

Rearranging Eq. (A1), we have $\zeta_a = \zeta + f = 2C_d r v^2 / [w_{\text{cool}}(r_0^2 - r^2)]$. Solving for r gives

$$r = \frac{-\xi_{E04}v^2 + \sqrt{\xi_{E04}^2v^4 + 4r_0^2}}{2},$$
 (A2)

with

$$\xi_{E04} = \frac{2C_d}{w_{\text{cool}}\zeta_a}.$$
 (A3)

It is seen that Eq. (16b) has the same form as Eq. (A2), with ξ playing the same role as ξ_{E04} , B playing the same role as $(1/2)w_{cool}$, f playing the same role as ζ_a , and $r_{RCE,eq}$ playing the same role as r_0 . In addition, B, having the dimension of velocity, is already in a form of Q_{cool} divided by stability; thus, B is also physically consistent with $(1/2)w_{cool}$. Taking the derivative of r with respect to v in Eq. (A2) will give the same form as Eq. (20).

Below, we show that the E04 model can show up in the same framework as in section 2, with a mass balance derivation. Considering the approximate mass balance in a cylinder from the TC center to r_t and from the surface to h_w :

$$\frac{1}{\alpha_p} M_{\text{ew}} - \pi r_t^2 w_{\text{cool}} \rho_w = -2\pi r_t \rho_i u_t h_w. \tag{A4}$$

Rearrangement gives

$$-u_{t} = \frac{1}{h_{w}} \frac{1}{2\pi} \frac{1}{\alpha_{p}} \left(\frac{M_{\text{ew}}}{\rho_{w}} \right) \frac{1}{r_{t}} - \frac{1}{h_{w}} \frac{1}{2} w_{\text{cool}} r_{t}$$

$$= \frac{1}{h_{w}} A_{\text{mb}} \left(\frac{M_{\text{ew}}}{\rho_{w}} \right) \frac{1}{r_{t}} - \frac{1}{h_{w}} B_{\text{mb}} r_{t}, \tag{A5}$$

where

$$A_{\rm mb} = \frac{1}{2\pi\alpha_p},\tag{A6a}$$

$$B_{\rm mb} = \frac{1}{2} w_{\rm cool}, \tag{A6b}$$

where the subscript "mb" means "mass balance." It is noticed that Eq. (A5) has the equivalent form as Eq. (10c), with A and B replaced by $A_{\rm mb}$ and $B_{\rm mb}$, respectively. The following derivation for dr/dt will be the same as in section 2. In particular, the equivalent counterpart of ξ will be $\xi_{\rm mb} = 2C_d\mu^2/(fw_{\rm cool})$, which more closely resembles ξ_{E04} .

APPENDIX B

Further Discussion on $\partial v/\partial r$ [Eq. (21)]

Equation (21) indicates that $\partial v/\partial r$ is negative definite and it tends to $-\infty$ when r_t tends to 0; $\partial v/\partial r$ tends to $-1/(\sigma \xi_0 v_t)$ when r_t tends to $+\infty$. Specifically, Eq. (21) gives

$$\frac{\partial}{\partial \xi_0} \left(\frac{\partial v}{\partial r} \Big|_{v = v_i} \right) = \frac{1}{\sigma \xi_0^2 v_i} > 0, \tag{B1}$$

which indicates that the magnitude of $\partial v/\partial r$ decreases with increased ξ_0 and vice versa. Physically, when C_d is increased or f is decreased, the magnitude of $\partial v/\partial r$ will decrease. Additionally, when $2r_t \gg \xi_0 v_t^2$, then $(\partial v/\partial r)^{-1}|_{v=v_t} \approx -2r_t v_t \sigma \xi_0/2r_t = -v_t \sigma \xi_0$, giving a proportional dependence of $\partial v/\partial r$ on fB/C_d . When $2r_t \ll \xi_0 v_t^2$, then $(\partial v/\partial r)^{-1}|_{v=v_t} \approx -2r_t \sigma/v_t$, proportional to r_t and independent of ξ_0 .

APPENDIX C

Experimental Design and Processing

Numerical experiments are performed with Cloud Model 1 (CM1; Bryan and Fritsch 2002), which is a nonhydrostatic model mainly designed for idealized simulations. The model configuration is essentially the same as Wang et al. (2022). The radiation is represented by applying a constant cooling rate $Q_{\rm cool}$ of potential temperature θ where the temperature is above a prescribed tropopause temperature $T_{\rm tpp}$. Where the temperature is lower than $T_{\rm tpp}$, the θ is relaxed to the value corresponding to $T_{\rm tpp}$ with a time scale $\tau=12$ h. A surface gustiness $u_{\rm sfc}=5$ m s⁻¹ is added to 10-m wind in the aerodynamic formula for surface drag and enthalpy fluxes. The Morrison double-moment microphysics scheme (Morrison et al. 2005) is used.

We set the environment in the CTL simulation as $T_{\text{tpp}} =$ 200 K, $T_{\text{SST}} = 300$ K, $f = 5 \times 10^{-5} \text{ s}^{-1}$, $C_d = C_k = 0.0015$, and $Q_{\text{cool}} = 1$ K day⁻¹. In the first set of experiments (TTPP; Table C1), we vary the tropopause temperature to vary V_p . This method has an advantage to isolate structural changes in the TC owing to changes of V_p without substantially affecting the lower-tropospheric properties, such as w_{cool} . To further test the role of C_d in modulating M_{ew} , two more sets of experiments CD and CDTTPP are designed (Table C1). In CD, C_d is varied, while in CDTTPP, C_d and $T_{\rm tpp}$ are both varied in a manner that V_p does not change (assuming the same air-sea enthalpy disequilibrium). The parameter C_k is further varied in CK (Table C1) to test whether $M_{\rm ew}$ is dominantly friction driven, as the boundary layer thermodynamic property is expected to change in CK. In the fifth set of experiments (FCOR, Table C1), we vary the Coriolis parameter f. In the sixth set of experiments (ExSST,

TABLE C1. Parameters in experiments.

TTPP		СДТТРР		CK	FCOR	ExSST
$T_{\text{tpp}}(K)$	C_d	$T_{\text{tpp}}(K)$	C_d	C_k	$f(10^{-5} \text{ s}^{-1})$	$T_{\rm SST}$ (K)
241	0.0031	241	0.0007	0.0007	_	_
227	0.0023	227	0.0010	0.0010	1.25	286
214	0.0019	214	0.0012	0.0012	2.5	293
200	0.0015	200	0.0015	0.0015	5	300
187	0.0012	187	0.0018	0.0018	10	307
174	0.0010	174	0.0022	0.0022	15	_
163	0.0009	163	0.0025	0.0025	_	_

Table C1), we vary $T_{\rm SST}$. Note that CD, CDTTPP, and CK will only be used for parameterizing $(M_{\rm ew}/\rho_w)_{\rm eq}$ (section 2d), with their equilibrium periods all set to 40–50 days.

TCs are simulated using the axisymmetric configuration of CM1, and the base state of the atmosphere is generated by three-dimensional simulations in radiative-convective equilibrium without the background rotation, same as Wang et al. (2022). In FCOR, CD, and CK, the base state of the atmosphere is all the same as the case with $T_{\rm tpp} = 200~{\rm K}$ in TTPP. TCs are simulated for 50 days in all simulations except 150 days for $f = 1.25 \times 10^{-5} \text{ s}^{-1}$ and 100 days for $f = 2.5 \times 10^{-5} \text{ s}^{-1}$ 10^{-5} s⁻¹ as the TCs with low f take longer to reach size equilibrium. The initial vortex for all experiments is the same and defined as in Rotunno and Emanuel (1987). The initial vortex maximum wind is about 13 m s⁻¹ at a radius of about 100 km; see also the supplemental material. For each value of the parameter being varied in TTPP, FCOR, and ExSST, we perform four ensemble simulations. We denote ensemble-index-0 as the ensemble member where the initial sounding outside of the vortex is not perturbed. For the other three ensemble members, the initial state of potential temperature over the whole domain is randomly perturbed with a maximum amplitude of 2.5 K ("irandp" = 1 in CM1 namelist) based on that of ensemble-index-0.

The eyewall upward mass flux is approximated by the inflow under the eyewall:

$$M_{\rm ew}(t) = -2\pi r_{\rm ew} \int_0^h \rho_d u \, dz, \tag{C1}$$

where $r_{\rm ew}$ is some radius not far from the eyewall (here chosen as two times $r_{u{\rm min}}$, the radius of the minimum radial velocity in the boundary layer), u is the radial velocity, and h is the height of the inflow layer, taken as the height where the radial velocity u is greater than 0.1 times the minimum u at $r_{\rm ew}$ (=2 $r_{u{\rm min}}$) following Zhang et al. (2011). The $M_{\rm ew}$ is processed by a 120-h running average. And ρ_w is calculated such that $-2\pi r_{\rm ew} - h \rho_w u_{\rm avg} = M_{\rm ew}$ in Eq. (C1), where $u_{\rm avg}$ is the vertical mean radial velocity of the inflow after 120-h running average and where \overline{h} is h after 120-h running average.

To evaluate Eqs. (1), (3), and (4), a spatial and temporal average is applied to remove noise in CM1 outputs:

$$\overline{[X]} = \frac{1}{z_2 - z_1} \int_{z_1}^{z_2} \left[\frac{2}{(r_t + \Delta r)^2 - (r_t - \Delta r)^2} \right] \\
\times \int_{r_t - \Delta r}^{r_t + \Delta r} \left(\frac{1}{P} \int_{t - P/2}^{t + P/2} X \, dt \right) r \, dr \, dz. \tag{C2}$$

This average $[\cdot]$ will apply to each term of Eq. (3): $\partial v/\partial t$ and u_t in Figs. 11–13, u_t in Figs. 14 and 15; $\Delta r = 100$ km, P = 120 h, $z_1 = 0$, and $z_2 = h_w = 2.5$ km are set. Note that one exception is that when applied to $\partial v/\partial r$ (Figs. 11–13): We take the central difference using two radii $r_t - \Delta r$ and $r_t + \Delta r$ of the 120-h temporal running average of v, at a fixed height 950 m, for smoother results. As $\partial v/\partial t$ and $\partial v/\partial r$ are very noisy, they are further applied to a 24-h

running average after applying $\overline{[\,\cdot\,]}$ in Figs. 11–13 for clearer visualization.

Quantity $w_{\rm cool}$ is calculated in the same manner as Wang et al. (2022). A typical value of $w_{\rm cool}$ is 0.0027 m s⁻¹ in the simulations. Quantity $Q_{\rm lat}$ from simulations (Figs. 9, 14, and 15) is also needed: $Q_{\rm lat}$ is calculated as the 120-h running average of the mass integration (radially within r_t) of $c_p\Pi\dot{\theta}_{\rm pc}$, with θ being the potential temperature, Π being the Exner function, and $\dot{\theta}_{\rm pc}$ being the potential temperature source due to phase changes (the tendency from the microphysics section provided by CM1 subtracted by the energy fallout term; see below). The height of the volume for the integration is defined as follows. First, the location of the maximum outflow velocity $u_{\rm max}$ of 120-h running averaged fields is found. The height of the volume is defined as 1 km above the height where the outflow velocity is less than 0.1 $u_{\rm max}$.

APPENDIX D

Support for Eq. (6) and Some Parameter Diagnosis and Interpretation

First, we provide a support of the dry-entropy balance equation Eq. (6). Recall that we define $s_d = c_p \ln(\theta/T_{\rm trip})$. Each term in Eq. (5) may be given as follows [see θ budget in Bryan and Rotunno (2009) and CM1 governing equations in the CM1 homepage], defining volume integration $\int_{0}^{z_f} = \int_{0}^{r_f} 2\pi r \, dr \, dz$:

$$\frac{\partial \mathcal{S}}{\partial t} = \int_{u} \frac{\partial \rho_d s_d}{\partial t},\tag{D1a}$$

$$\begin{split} \frac{\mathcal{Q}_{\text{lat}}}{T_{e,\text{lat}}} &= \int_{v} \left\{ \rho_{d} \left[-\frac{c_{v}}{c_{vm}} \left(\frac{L_{v}}{T} \ \dot{q}_{gl} + \frac{L_{f}}{T} \ \dot{q}_{ls} + \frac{L_{s}}{T} \ \dot{q}_{gs} \right) \right. \\ &+ \left. \left(\frac{c_{v}}{c_{vm}} - \frac{R}{R_{m}} \right) R_{v} (\dot{q}_{gl} + \dot{q}_{gs}) \right] \right\}, \end{split} \tag{D1b}$$

$$-\frac{Q_{\rm rad}}{T_{e,\rm rad}} = \int_{\nu} \left(\rho_d \, \frac{c_p}{\theta} \, \dot{\theta}_{\rm rad} \right), \tag{D1c}$$

$$\dot{S}_{\text{res}} = \int_{v} -\rho_{d} \left(\frac{c_{v}}{c_{vm}} R_{m} - R \right) \nabla \mathbf{u} + \int_{v} -\frac{c_{v}}{c_{vm}} \frac{\nabla \mathbf{J}}{T} + \int_{v} \frac{c_{v}}{c_{vm}} \frac{1}{T} (W_{T} + \epsilon),$$
 (D1d)

$$\mathcal{F}_{r} = \int_{0}^{z_{l}} -2\pi r_{l}(\rho_{d}us_{d})|_{r=r_{l}} dz,$$
 (D1e)

$$\mathcal{F}_u = \int_0^{r_t} -2\pi r (\rho_d w s_d)|_{z=z_t} dr, \tag{D1f}$$

where c_v is the specific heat of dry air at constant volume; $c_{vm} = c_v + c_{vv}q_v + c_lq_l + c_sq_s$, with c_{vv} , c_l , and c_s being the specific heat of water vapor, liquid water, and solid water at

¹⁶ Quantity w_{cool} was incorrectly calculated to be about half of the correct value in Wang et al. (2022).

constant volume, respectively, and q_l and q_s are the mixing ratios of liquid water and solid water, respectively; R is the gas constant of dry air, $R_m = R + q_v R_v$ is the gas constant of moist air, with R_v being the gas constant of water vapor; L_v , L_f , and L_s are the latent heat of vaporization, freezing, and sublimation, respectively; \dot{q}_{gl} and \dot{q}_{gs} are the q_v source from phase changes between gas and liquid water and gas and solid water, respectively; \dot{q}_{ls} is the q_l source from phase changes between liquid and solid water; $\dot{\theta}_{rad}$ is the θ source due to radiative cooling; vector \mathbf{u} is the velocity; vector \mathbf{J} is the sensible heat flux per unit area; W_T is the heating/cooling rate per unit volume due to falling hydrometeors; and ϵ is the dissipative heating. In particular, $W_T = -c_{nn}\mathbf{d}_n\nabla T$ $c_l \mathbf{d}_l \nabla T - c_s \mathbf{d}_s \nabla T + \mathbf{g} \cdot (\mathbf{d}_v + \mathbf{d}_l + \mathbf{d}_s)$, where \mathbf{d}_v , \mathbf{d}_l , and \mathbf{d}_s are the diffusion (fall out) fluxes of water vapor, liquid water, and solid water per unit area, respectively (see also appendix A of Romps 2008; Wang and Lin 2021), and g is the gravitational acceleration.

In practice, Eq. (D1) in a CM1 simulation is obtained by its automatic output of θ budget. Specifically, $Q_{\rm lat}/T_{e,\rm lat}$ is obtained from the CM1 output "ptb_mp" (θ source from the microphysics section) subtracted by the effect of W_T using the CM1 output of the terminal fall speed of different hydrometeors. Note, in particular, that ptb_mp itself can be a close approximation of θ source due to phase changes because a simple scale estimation gives that the dry-entropy source due to W_T [Eq. (D1d)] is only a few percent of that due to phase changes [Eq. (D1b)], assuming $\partial T/\partial z = -7$ K km⁻¹ and a mean condensation height (for the vertical distance of falling) of 3 km (this estimation is supported by explicit diagnosis not shown).

Figures D1a and D1b show the support of the approximation given by Eq. (6) by representative cases of CTL and $T_{\rm tpp}=163$ K case in TTPP. It is evident that the local tendency $\partial S/\partial t$, dry-entropy source $\dot{S}_{\rm res}$, and vertical flux \mathcal{F}_u are indeed negligible with dominant terms $\mathcal{Q}_{\rm lat}/T_{e,{\rm lat}}$, \mathcal{F}_r and $-\mathcal{Q}_{\rm rad}/T_{e,{\rm rad}}$, which is important when TC is large. The crucial assumption/approximation that $\mathcal{Q}_{\rm lat}/T_{e,{\rm lat}}$ scales with r_t and $\mathcal{Q}_{\rm rad}/T_{e,{\rm rad}}$ scales with r_t^2 is more clearly (than in the main text) supported by Figs. D1c-f for TTPP and FCOR (similar for ExSST, not shown).

In section 3, we set $\alpha_p = 0.8$, $\epsilon_{p,\text{ew}} = 1$; here, some support for this setting is shown in Fig. D2. Consistent with the definition in section 2a, α_p is calculated as the ratio between the latent heating within two times the radius of maximum wind r_m and Q_{lat} . Two times of r_m is to account for the slope of the eyewall, which could also include some inner rainband according to Wang (2009). It is seen that α_p in TTPP and ExSST is approximately constant being about 0.7-0.8, suggesting the dominant contribution of latent heating in the eyewall to total latent heating within r_8 . In FCOR, however, it is seen that α_p can be substantially smaller when $f = 2.5 \times 10^{-5}$ and $f = 1.25 \times 10^{-5}$ s⁻¹, indicating that latent heating outside of the eyewall is important in driving the expansion of these cases. It is also noted that when $f = 2.5 \times 10^{-5} \text{ s}^{-1}$, α_p is still mainly above 0.6 when r_8 is smaller than 1000 km, a radius more relevant to TCs on Earth.

Here, for convenience, $\epsilon_{p,\mathrm{ew}}$ is diagnosed/estimated as the ratio of 120-h running averaged precipitation to the 120-h running averaged sum of surface water vapor and lateral water (vapor and hydrometeors) fluxes within (at) two times of r_m . Note $\epsilon_{p,\mathrm{ew}}$ thus defined is similar to the large-scale precipitation efficiency in Sui et al. (2005). It is seen in Figs. D2d-f that $\epsilon_{p,\mathrm{ew}}$ is about 1 during the whole expansion stage. This indicates a negligible local accumulation of water in the atmosphere, and nearly all water vapor input to the eyewall changes phase.

We also show Δs_d diagnosed by Eq. (7) in simulations in Fig. D3. It is seen that the diagnosed Δs_d is approximately constant with time in TTPP, FCOR, and ExSST. The diagnosed Δs_d is very close in different experiments of TTPP and FCOR; the value is also not far from the 187.1 J K⁻¹ kg⁻¹ estimation in the ideal base environment in section 3. The diagnosed Δs_d in ExSST also matches well with the expansion model, following the C–C scaling. This supports our assumption of a constant Δs_d and directly supports the interpretation of Δs_d . Our assumption that Δs_d is mainly driven by sea surface temperature is verified. Note the diagnosed Δs_d slightly increases with decreasing $T_{\rm tpp}$; this also means the faster expansion rate with lower $T_{\rm tpp}$ is not caused by a Δs_d sensitivity.

The meaning of Δs_d may be further understood in a more ideal picture where the inflow at r_t occurs only from the surface to the height z_i and the outflow only occurs from z_i to z_l and where $z_i \lesssim z_l$ so that the outflow is well confined to the tropopause level. To simplify the math, we also assume that the buoyancy frequency N is a constant so that $\partial s_d/\partial z = (c_p/g)N^2$ is a constant (not a bad approximation as seen in CTL; see the supplemental material). We denote s_d at the surface to be s_{d0} so that $s_{di} = s_{d0} + (c_p/g)N^2z_i$ is the s_d at height z_i ; we denote $s_{d,tpp}$ the s_d at height z_l . Thus, \mathcal{F}_r [Eq. (D1e)] is written as

$$\mathcal{F}_{r} = \int_{0}^{z_{i}} -2\pi r_{t}(\rho_{d}us_{d})dz + \int_{z_{i}}^{z_{t}} -2\pi r_{t}(\rho_{d}us_{d})dz$$
 (D2)

The first term on the RHS is written as

$$\begin{split} & \int_{0}^{z_{i}} -2\pi r_{t}(\rho_{d}us_{d})dz \\ & = -2\pi r_{t} \int_{0}^{z_{i}} \rho_{d}u \left(s_{d0} + \frac{c_{p}}{g} N^{2}z\right) dz \\ & = s_{d0} \left(-2\pi r_{t} \int_{0}^{z_{i}} \rho_{d}u \, dz\right) - 2\pi r_{t} \frac{c_{p}}{g} N^{2} \int_{0}^{z_{i}} \rho_{d}uz \, dz \\ & = s_{d0}\psi_{i} + \frac{c_{p}}{g} N^{2} \int_{0}^{z_{i}} \frac{\partial \psi}{\partial z} z \, dz \\ & = s_{d0}\psi_{i} + \frac{c_{p}}{g} N^{2} \left[(\psi z) \right]_{0}^{z_{i}} - \int_{0}^{z_{i}} \psi \, dz \right] \\ & = s_{d0}\psi_{i} + \frac{c_{p}}{g} N^{2}\psi_{i}z_{i} - \frac{c_{p}}{g} N^{2} \int_{0}^{z_{i}} \psi \, dz \\ & = s_{di}\psi_{i} - \frac{c_{p}}{g} N^{2} \int_{0}^{z_{i}} \psi \, dz, \end{split} \tag{D3}$$

where ψ is the mass streamfunction. The second term on the RHS of Eq. (D2) is written as

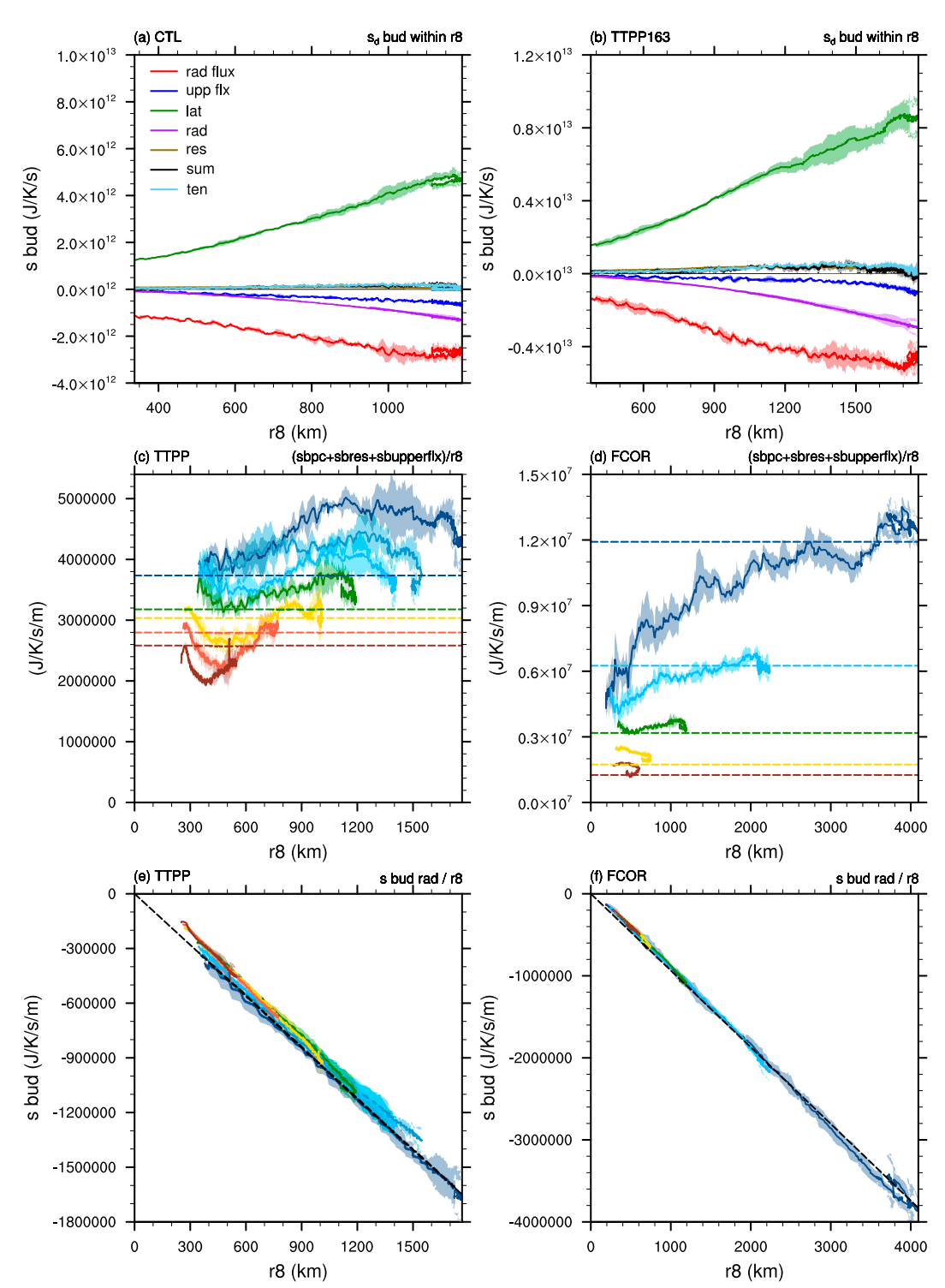


FIG. D1. (a),(b) Terms in the dry-entropy budget Eq. (D1) (J K $^{-1}$ s $^{-1}$) in CTL and the $T_{\rm tpp}=163$ K case in TTPP; legend shows (from top to bottom) terms \mathcal{F}_r , \mathcal{F}_u , $\mathcal{Q}_{\rm lat}/T_{e,\rm lat}$, $-(\mathcal{Q}_{\rm rad}/T_{e,\rm rad})$, $\dot{\mathcal{S}}_{\rm res}$, $\partial S/\partial t$ as the sum of these terms and directly calculated (solid lines: ensemble mean; shading: one standard deviation). (c),(d) The equation $[(\mathcal{Q}_{\rm lat}/T_{e,\rm lat})+\dot{\mathcal{S}}_{\rm res}+\mathcal{F}_u]/r_8$ (J K $^{-1}$ s $^{-1}$ m $^{-1}$) in TTPP and FCOR (solid lines: ensemble mean; shading: one standard deviation), respectively. Warmer color means higher values of $T_{\rm tpp}$ or f; dashed lines mark the expansion model predictions in section 4. (e),(f) As in (c) and (d), but for $-(\mathcal{Q}_{\rm rad}/T_{e,\rm lat})/r_8$ (J K $^{-1}$ s $^{-1}$ m $^{-1}$).

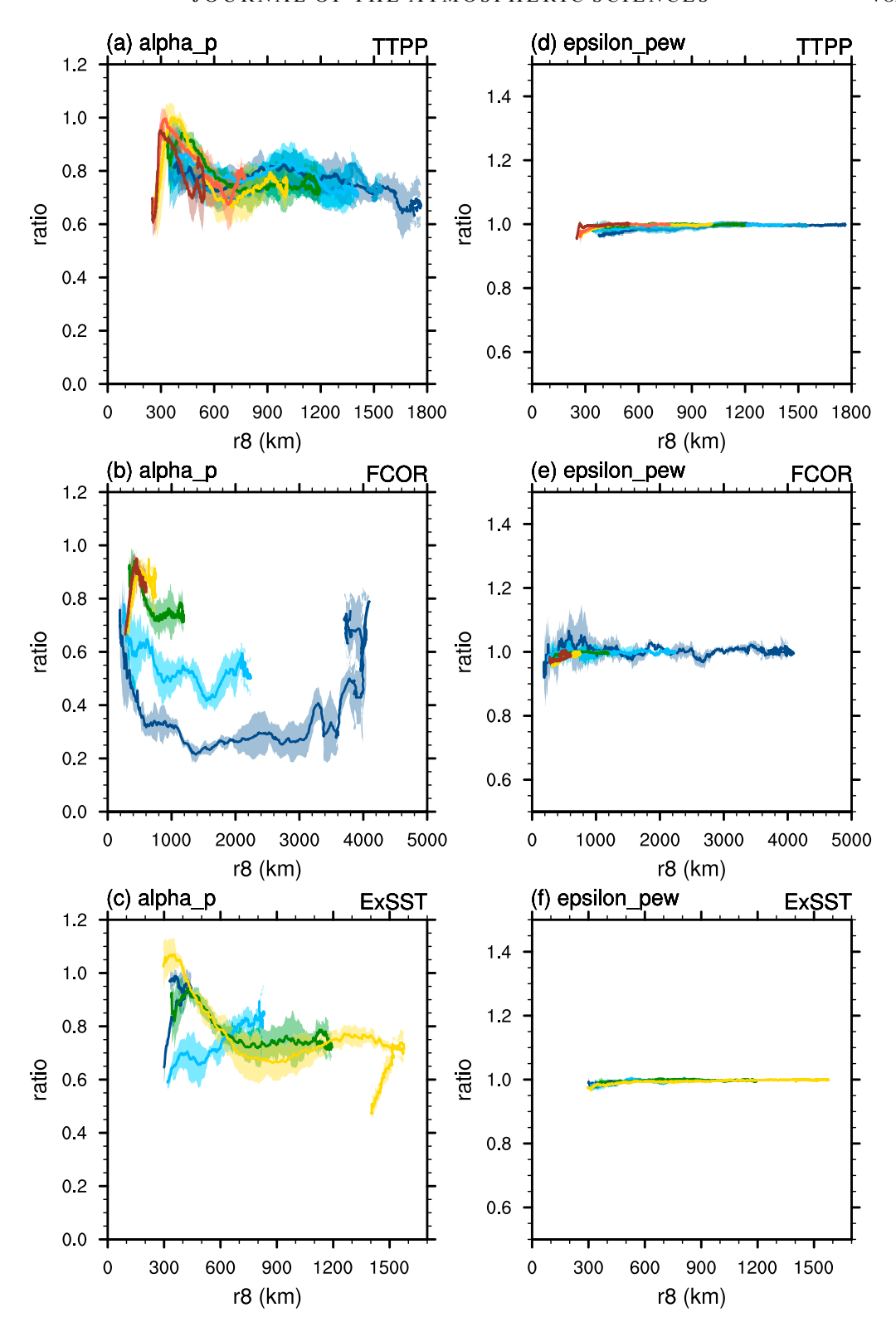


FIG. D2. (a)–(c) Diagnosed α_p (solid lines: ensemble mean; shading: one standard deviation) as a function of r_8 in TTPP, FCOR, and ExSST, respectively. (d)–(f) As in (a)–(c), but for $\epsilon_{p,\text{ew}}$. Warmer colors mean higher values of the variable being varied. See the text for details.

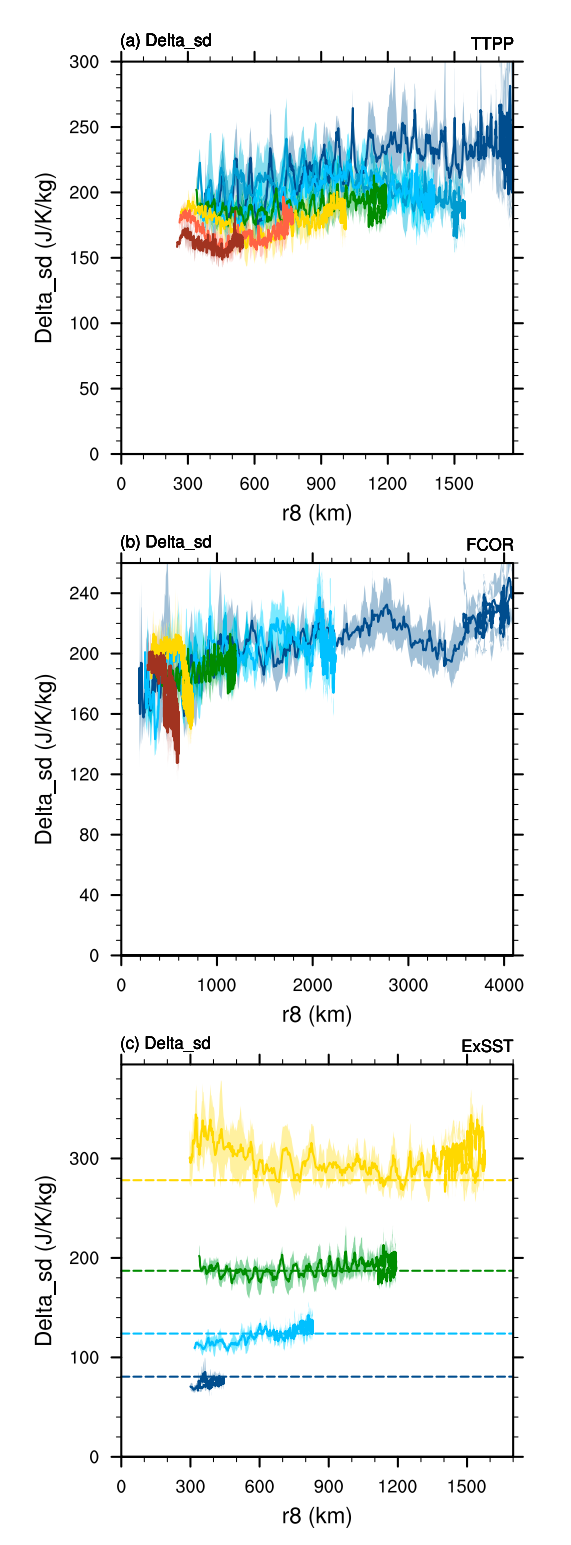


FIG. D3. Diagnosed Δs_d (J K⁻¹ kg⁻¹; solid lines: ensemble mean; shading: one standard deviation) in (a) TTPP, (b) FCOR, and (c) ExSST using Eq. (7). Colors have the same meaning as Fig. D2. Note in the calculation, the numerator and denominator of Eq. (7) are first processed by a 120-h running average. Dashed lines in (c) show the expansion model predicted $\Delta s_d = L_v q_{vs}^*/T_s$, which are also used in section 4.

$$\int_{z_t}^{z_t} -2\pi r_t(\rho_d u s_d) dz = \int_{z_t}^{z_t} \frac{\partial \psi}{\partial z} s_d dz \approx s_{di}(-\psi_i).$$
 (D4)

Thus, we have $\mathcal{F}_r = -(c_p/g)N^2\int_0^{z_i}\psi\,dz = -(c_p/g)N^2\overline{\psi}z_i$. Note also that $2\pi r_t\rho_iu_th_w = -\psi_{h_w}$. Then, Δs_d [Eq. (7)] is

$$\begin{split} \Delta s_d &= \mathcal{F}_r / (-\psi_{h_w}) \\ &= \frac{c_p}{g} \ N^2 z_i \ \frac{\overline{\psi}}{\psi_{h_w}} \\ &\approx (s_{d,\mathrm{tpp}} - s_{d0}) \frac{\overline{\psi}}{\psi_h} \,. \end{split} \tag{D5}$$

Thus, we see that Δs_d will represent the difference of s_d between tropopause and the surface if $\psi_{h_{\tilde{k}}}$ is close to the vertical mean of ψ in the whole inflow layer. A structure with the inflow confined near the surface satisfies this condition, but other vertical profiles of the inflow can also be valid.

REFERENCES

Bryan, G. H., and J. M. Fritsch, 2002: A benchmark simulation for moist nonhydrostatic numerical models. *Mon. Wea. Rev.*, **130**, 2917–2928, https://doi.org/10.1175/1520-0493(2002)130 <2917:ABSFMN>2.0.CO;2.

—, and R. Rotunno, 2009: The maximum intensity of tropical cyclones in axisymmetric numerical model simulations. *Mon. Wea. Rev.*, 137, 1770–1789, https://doi.org/10.1175/2008MWR2709.1.

Bu, Y. P., R. G. Fovell, and K. L. Corbosiero, 2014: Influence of cloud–radiative forcing on tropical cyclone structure. *J. At*mos. Sci., 71, 1644–1662, https://doi.org/10.1175/JAS-D-13-0265.1.

—, —, and —, 2017: The influences of boundary layer mixing and cloud-radiative forcing on tropical cyclone size. *J. Atmos. Sci.*, **74**, 1273–1292, https://doi.org/10.1175/JAS-D-16-0231.1.

Bui, H. H., R. K. Smith, T. Montgomery, and J. Peng, 2009: Balanced and unbalanced aspects of tropical cyclone intensification. *Quart. J. Roy. Meteor. Soc.*, 135, 1715–1731, https://doi.org/10.1002/qj.502.

Chan, K. T., and J. C. Chan, 2014: Impacts of initial vortex size and planetary vorticity on tropical cyclone size. *Quart. J. Roy. Meteor. Soc.*, 140, 2235–2248, https://doi.org/10.1002/qj.2292.

—, and —, 2015: Impacts of vortex intensity and outer winds on tropical cyclone size. *Quart. J. Roy. Meteor. Soc.*, **141**, 525–537, https://doi.org/10.1002/qj.2374.

Chan, K. T. F., and J. C. L. Chan, 2018: The outer-core wind structure of tropical cyclones. J. Meteor. Soc. Japan, 96, 297– 315, https://doi.org/10.2151/jmsj.2018-042.

Chavas, D. R., and K. Emanuel, 2014: Equilibrium tropical cyclone size in an idealized state of axisymmetric radiative–convective equilibrium. *J. Atmos. Sci.*, 71, 1663–1680. https://doi.org/10. 1175/JAS-D-13-0155.1.

—, and N. Lin, 2016: A model for the complete radial structure of the tropical cyclone wind field. Part II: Wind field variability. J. Atmos. Sci., 73, 3093–3113, https://doi.org/10.1175/JAS-D-15-0185.1.

—, and K. A. Reed, 2019: Dynamical aquaplanet experiments with uniform thermal forcing: System dynamics and implications

- for tropical cyclone genesis and size. *J. Atmos. Sci.*, **76**, 2257–2274, https://doi.org/10.1175/JAS-D-19-0001.1.
- —, and J. A. Knaff, 2022: A simple model for predicting the tropical cyclone radius of maximum wind from outer size. Wea. Forecasting, 37, 563–579, https://doi.org/10.1175/WAF-D-21-0103.1.
- —, N. Lin, and K. Emanuel, 2015: A model for the complete radial structure of the tropical cyclone wind field. Part I: Comparison with observed structure. J. Atmos. Sci., 72, 3647– 3662, https://doi.org/10.1175/JAS-D-15-0014.1.
- Dunion, J. P., 2011: Rewriting the climatology of the tropical North Atlantic and Caribbean Sea atmosphere. *J. Climate*, 24, 893–908, https://doi.org/10.1175/2010JCLI3496.1.
- Emanuel, K., 2004: Tropical cyclone energetics and structure. Atmospheric Turbulence and Mesoscale Meteorology, Cambridge University Press, 165–191, https://doi.org/10.1017/CBO9780511735035.010.
- ——, 2012: Self-stratification of tropical cyclone outflow. Part II: Implications for storm intensification. *J. Atmos. Sci.*, **69**, 988–996, https://doi.org/10.1175/JAS-D-11-0177.1.
- —, and R. Rotunno, 2011: Self-stratification of tropical cyclone outflow. Part I: Implications for storm structure. *J. Atmos. Sci.*, 68, 2236–2249, https://doi.org/10.1175/JAS-D-10-05024.1.
- Emanuel, K. A., 1986: An air-sea interaction theory for tropical cyclones. Part I: Steady-state maintenance. *J. Atmos. Sci.*, **43**, 585–605, https://doi.org/10.1175/1520-0469(1986)043<0585: AASITF>2.0.CO;2.
- —, 1988: The maximum intensity of hurricanes. J. Atmos. Sci., 45, 1143–1155, https://doi.org/10.1175/1520-0469(1988)045<1143: TMIOH>2.0.CO;2.
- ——, 1991: The theory of hurricanes. Annu. Rev. Fluid Mech., 23, 179–196, https://doi.org/10.1146/annurev.fl.23.010191.001143.
- —, 1995: The behavior of a simple hurricane model using a convective scheme based on subcloud-layer entropy equilibrium. J. Atmos. Sci., 52, 3960–3968, https://doi.org/10.1175/1520-0469 (1995)052<3960:TBOASH>2.0.CO;2.
- Fudeyasu, H., Y. Wang, M. Satoh, T. Nasuno, H. Miura, and W. Yanase, 2010: Multiscale interactions in the life cycle of a tropical cyclone simulated in a global cloud-system-resolving model. Part II: System-scale and mesoscale processes. *Mon. Wea. Rev.*, 138, 4305–4327, https://doi.org/10.1175/2010MWR3475.1.
- Hill, K. A., and G. M. Lackmann, 2009: Influence of environmental humidity on tropical cyclone size. *Mon. Wea. Rev.*, 137, 3294–3315, https://doi.org/10.1175/2009MWR2679.1.
- Kepert, J., 2001: The dynamics of boundary layer jets within the tropical cyclone core. Part I: Linear theory. J. Atmos. Sci., 58, 2469–2484, https://doi.org/10.1175/1520-0469(2001)058<2469: TDOBLJ>2.0.CO;2.
- Khairoutdinov, M., and K. Emanuel, 2013: Rotating radiative-convective equilibrium simulated by a cloud-resolving model. J. Adv. Model. Earth Syst., 5, 816–825, https://doi.org/10.1002/2013MS000253.
- Kossin, J. P., and M. Sitkowski, 2009: An objective model for identifying secondary eyewall formation in hurricanes. *Mon. Wea. Rev.*, 137, 876–892, https://doi.org/10.1175/2008MWR2701.1.
- Kuo, H. L., 1982: Vortex boundary layer under quadratic surface stress. Bound.-Layer Meteor., 22, 151–169, https://doi.org/10. 1007/BF00118250.
- Li, Y., Y. Wang, Y. Lin, and R. Fei, 2020: Dependence of superintensity of tropical cyclones on SST in axisymmetric numerical simulations. *Mon. Wea. Rev.*, 148, 4767–4781, https://doi.org/10.1175/MWR-D-20-0141.1.

- —, and Z. Tan, 2023: Is the outflow-layer inertial stability crucial to the energy cycle and development of tropical cyclones?. J. Atmos. Sci., 80, 1605–1620, https://doi.org/10.1175/ JAS-D-22-0186.1.
- Lu, K.-Y., and D. R. Chavas, 2022: Tropical cyclone size is strongly limited by the Rhines scale: Experiments with a barotropic model. *J. Atmos. Sci.*, 79, 2109–2124, https://doi.org/ 10.1175/JAS-D-21-0224.1.
- Maclay, K. S., M. DeMaria, and T. H. Vonder Haar, 2008: Tropical cyclone inner-core kinetic energy evolution. *Mon. Wea. Rev.*, 136, 4882–4898, https://doi.org/10.1175/2008MWR2268.1.
- Martinez, J., C. C. Nam, and M. M. Bell, 2020: On the contributions of incipient vortex circulation and environmental moisture to tropical cyclone expansion. *J. Geophys. Res. Atmos.*, 125, e2020JD033324, https://doi.org/10.1029/2020JD033324.
- Morrison, H., J. A. Curry, and V. I. Khvorostyanov, 2005: A new double-moment microphysics parameterization for application in cloud and climate models. Part I: Description. J. Atmos. Sci., 62, 1665–1677, https://doi.org/10.1175/JAS3446.1.
- Pauluis, O., V. Balaji, and I. M. Held, 2000: Frictional dissipation in a precipitating atmosphere. J. Atmos. Sci., 57, 989–994, https://doi.org/10.1175/1520-0469(2000)057<0989:FDIAPA> 2.0.CO;2.
- Peng, K., R. Rotunno, and G. H. Bryan, 2018: Evaluation of a time-dependent model for the intensification of tropical cyclones. J. Atmos. Sci., 75, 2125–2138, https://doi.org/10.1175/ JAS-D-17-0382.1.
- Persing, J., and M. T. Montgomery, 2003: Hurricane superintensity. J. Atmos. Sci., 60, 2349–2371, https://doi.org/10.1175/1520-0469(2003)060<2349:HS>2.0.CO;2.
- —, —, R. K. Smith, and J. C. McWilliams, 2019: Quasi steady-state hurricanes revisited. *Trop. Cyclone Res. Rev.*, **8** (1), 1–17, https://doi.org/10.1016/j.tcrr.2019.07.001.
- Ramsay, H. A., M. S. Singh, and D. R. Chavas, 2020: Response of tropical cyclone formation and intensification rates to climate warming in idealized simulations. *J. Adv. Model. Earth Syst.*, 12, e2020MS002086, https://doi.org/10.1029/2020MS002086.
- Raymond, D. J., S. L. Sessions, A. H. Sobel, and Ž. Fuchs, 2009: The mechanics of gross moist stability. *J. Adv. Model. Earth Syst.*, 1(3), https://doi.org/10.3894/JAMES.2009.1.9.
- Romps, D. M., 2008: The dry-entropy budget of a moist atmosphere. J. Atmos. Sci., 65, 3779–3799, https://doi.org/10.1175/2008JAS2679.1.
- —, 2016: Clausius–clapeyron scaling of cape from analytical solutions to RCE. *J. Atmos. Sci.*, 73, 3719–3737, https://doi.org/10.1175/JAS-D-15-0327.1.
- Rotunno, R., and K. A. Emanuel, 1987: An air-sea interaction theory for tropical cyclones. Part II: Evolutionary study using a nonhydrostatic axisymmetric numerical model. *J. Atmos. Sci.*, 44, 542–561, https://doi.org/10.1175/1520-0469(1987)044<0542: AAITFT>2.0.CO;2.
- Schenkel, B. A., N. Lin, D. Chavas, G. A. Vecchi, M. Oppenheimer, and A. Brammer, 2018: Lifetime evolution of outer tropical cyclone size and structure as diagnosed from reanalysis and climate model data. *J. Climate*, 31, 7985–8004, https://doi.org/10.1175/JCLI-D-17-0630.1.
- —, D. Chavas, N. Lin, T. Knutson, G. Vecchi, and A. Brammer, 2023: North Atlantic tropical cyclone outer size and structure remain unchanged by the late twenty-first century. *J. Climate*, 36, 359–382, https://doi.org/10.1175/JCLI-D-22-0066.1.
- Smith, R. K., G. Kilroy, and M. T. Montgomery, 2015: Why do model tropical cyclones intensify more rapidly at low latitudes?.

- J. Atmos. Sci., 72, 1783–1804, https://doi.org/10.1175/JAS-D-14-00441.
- Stern, D. P., G. H. Bryan, and S. D. Aberson, 2016: Extreme low-level updrafts and wind speeds measured by dropsondes in tropical cyclones. *Mon. Wea. Rev.*, 144, 2177–2204, https://doi.org/10.1175/MWR-D-15-0313.1.
- Sui, C.-H., X. Li, M.-J. Yang, and H.-L. Huang, 2005: Estimation of oceanic precipitation efficiency in cloud models. *J. Atmos. Sci.*, **62**, 4358–4370, https://doi.org/10.1175/JAS3587.1.
- Tsuji, H., H. Itoh, and K. Nakajima, 2016: Mechanism governing the size change of tropical cyclone-like vortices. *J. Meteor. Soc. Japan*, **94**, 219–236, https://doi.org/10.2151/jmsj.2016-012.
- Wang, D., and Y. Lin, 2021: Potential role of irreversible moist processes in modulating tropical cyclone surface wind structure. J. Atmos. Sci., 78, 709–725, https://doi.org/10.1175/JAS-D-20-0192.1.
- ——, and D. R. Chavas, 2022: Tropical cyclone potential size. J. Atmos. Sci., 79, 3001–3025, https://doi.org/10.1175/ JAS-D-21-0325.1.
- Wang, S., and R. Toumi, 2022: An analytic model of the tropical cyclone outer size. npj Climate Atmos. Sci., 5, 46, https://doi. org/10.1038/s41612-022-00270-6.
- Wang, Y., 2009: How do outer spiral rainbands affect tropical cyclone structure and intensity? *J. Atmos. Sci.*, 66, 1250–1273, https://doi.org/10.1175/2008JAS2737.1.

- —, Y. Li, and J. Xu, 2021a: A new time-dependent theory of tropical cyclone intensification. *J. Atmos. Sci.*, 78, 3855–3865, https://doi.org/10.1175/JAS-D-21-0169.1.
- —, —, Z.-M. Tan, and Y. Lin, 2021b: The intensity dependence of tropical cyclone intensification rate in a simplified energetically based dynamical system model. *J. Atmos. Sci.*, **78**, 2033–2045, https://doi.org/10.1175/JAS-D-20-0393.1.
- Weatherford, C., and W. Gray, 1988: Typhoon structure as revealed by aircraft reconnaissance. Part I: Data analysis and climatology. *Mon. Wea. Rev.*, **116**, 1032–1043, https://doi.org/10.1175/1520-0493(1988)116<1032:TSARBA>2.0.CO;2.
- Xi, D., S. Wang, and N. Lin, 2023: Analyzing relationships between tropical cyclone intensity and rain rate over the ocean using numerical simulations. *J. Climate*, 36, 81–91, https://doi.org/10.1175/JCLI-D-22-0141.1.
- Xu, J., and Y. Wang, 2010: Sensitivity of the simulated tropical cyclone inner-core size to the initial vortex size. *Mon. Wea. Rev.*, 138, 4135–4157, https://doi.org/10.1175/2010MWR3335.1.
- Zhang, J. A., R. F. Rogers, D. S. Nolan, and F. D. Marks, 2011: On the characteristic height scales of the hurricane boundary layer. *Mon. Wea. Rev.*, 139, 2523–2535, https://doi.org/10. 1175/MWR-D-10-05017.1.